

Chemical heterogeneity, convection and asymmetry beneath mid-ocean ridges

Adina E. Pusok,¹ Richard F. Katz,¹ Dave A. May² and Yuan Li¹

¹*Department of Earth Sciences, University of Oxford, Oxford OX1 3AN, United Kingdom. E-mail: adina.pusok@earth.ox.ac.uk*

²*Scripps Institution of Oceanography, Institute of Geophysics and Planetary Physics, UC San Diego, La Jolla, CA 92037, USA*

Accepted 2022 August 6. Received 2022 May 3; in original form 2022 July 26

SUMMARY

Geophysical observations at some mid-ocean ridges document an across-axis asymmetry in indicators of magma production. Other observations are interpreted as showing non-monotonic variations in the depth of the lithosphere–asthenosphere boundary. These patterns are inconsistent with the classical models of mantle corner flow and half-space cooling. To investigate this discrepancy, we use models of coupled magma/mantle dynamics beneath mid-ocean ridges in which phase densities are determined by melt–residue partitioning of iron and magnesium, and bulk density is affected by residual porosity. Our models predict that emergent gradients in density drive ridge-local convection. In particular, we show that convective upwelling is enhanced by porous buoyancy and suppressed by compositional buoyancy. Despite this suppression, models that include both compositional and porous buoyancy are more sensitive to long-wavelength mantle heterogeneity than models with porous buoyancy alone. This sensitivity enables models to readily form across-axis asymmetry of upwelling. In some cases, it leads to lithospheric delamination and time-dependent, small-scale convection. We conclude that melting-induced buoyancy effects may explain the magmatic asymmetry and variations in lithospheric thickness that are inferred from observations.

Key words: Mantle processes; Numerical modelling; Dynamics of lithosphere and mantle; Mid-ocean ridge processes; Magma genesis and partial melting.

1 INTRODUCTION

In the classical understanding, mid-ocean ridges (MORs) are tectonic boundaries where local mantle upwelling is driven by plate divergence, and where the oceanic lithosphere forms by conductive cooling as it moves away from the ridge (McKenzie 1969; Phipps Morgan *et al.* 1987). In this passive-flow model, a symmetrical and roughly triangular partial-melt zone is predicted to form beneath the ridge axis. The plate spreading rate is then the key factor determining the rate of mantle flow, associated melting and plate characteristics (Phipps Morgan *et al.* 1987; Parmentier & Phipps Morgan 1990; Olive & Dublanche 2020; White *et al.* 2001). In particular, the fairly uniform MOR basalt (MORB) chemistry (e.g. McKenzie & Bickle 1988; Langmuir *et al.* 1992) implies a generic melting process across the global ridge system (Hofmann 1997); this has favoured the simpler theory of passive mantle flow beneath ridges (Spiegelman & Reynolds 1999). However, much of the diversity of the ridge system cannot be explained by spreading rate alone (e.g. Small & Danyushevsky 2003; Rubin & Sinton 2007; Rychert *et al.* 2020), whilst a number of observations indicate symmetry-breaking behaviour and deviations from the passive-flow model.

1.1 Observations of asymmetry beneath MORs

Geophysical observations of MORs indicate asymmetry in melt production and upwelling across the ridge axis (Melt Seismic Team 1998; Rychert *et al.* 2020). The MELT (Forsyth & Chave 1994; Forsyth *et al.* 1998) and the GLIMPSE experiments (Forsyth *et al.* 2006) found pronounced asymmetry in mantle structure beneath the East Pacific Rise. For example, comparing the regions west and east of the rise, the west is characterized by slower seafloor subsidence (Cochran 1986), faster absolute plate motion in the hotspot reference frame (Gripp & Gordon 1990), more abundant seamounts (Scheirer *et al.* 1998), less dense mantle (Cormier *et al.* 1995; Scheirer *et al.* 1998; Canales *et al.* 1998), greater shear wave splitting (Wolfe & Solomon 1998), lower seismic velocities (Forsyth *et al.* 1998) and higher electrical conductivity (Evans *et al.* 1999). The seismically slow region of mantle was interpreted as a zone of partial melting with porosity $\sim 1\%$ (Toomey *et al.* 1998) that is not associated with a deep root of anomalously hot or buoyant mantle (Forsyth *et al.* 1998; Melt Seismic Team 1998).

Similar asymmetry has also been found at intermediate-spreading centres such as Juan de Fuca ridge (Toomey *et al.* 2014; Bell *et al.* 2016), Pacific–Antarctic Ridge (Vlastélic *et al.* 1999) and the

Mid-Atlantic Ridge (Wang *et al.* 2020), and at slow-spreading centres such as the Mohs Ridge (Johansen *et al.* 2019) and the Gulf of California rift zone (Wang *et al.* 2009). At the Juan de Fuca ridge, early studies documented an asymmetry in the distribution of seamounts close to the ridge (e.g. McManus 1967; Mammerickx & Taylor 1971; Davis & Karsten 1986). Because the Juan de Fuca ridge is migrating westward in the absolute hotspot reference frame at $\sim 2 \text{ cm yr}^{-1}$ and the Juan de Fuca Plate is nearly stationary, Davis & Karsten (1986) originally proposed that ridge migration causes the seamount asymmetry. However, recent gravity (Marjanovic *et al.* 2011) and seismic (Toomey *et al.* 2014; Bell *et al.* 2016) investigations revealed that the asymmetry extends below the ridge in a pronounced low-velocity, partial-melt zone that cannot be attributed to plate migration.

1.2 Observations of deviations from the half-space cooling model of lithosphere

A second prediction of the passive flow model is the conductive cooling of the lithosphere with age [i.e. half-space cooling model, Turcotte & Schubert (2014)]. Observations such as heat flow, seafloor bathymetry, elastic thickness estimates, seismic imaging and magnetotelluric (MT) imaging support an age progression in lithospheric thickness between the youngest and the oldest seafloor (e.g. Parsons & Sclater 1977; Turcotte & Schubert 2014). However, seismic and electromagnetic studies have also inferred variations in the lithosphere–asthenosphere boundary (LAB) and plate thicknesses that are uncorrelated with plate age (e.g. Forsyth *et al.* 1998; Kawakatsu *et al.* 2009; Rychert & Shearer 2009; Naif *et al.* 2013; Key *et al.* 2013; Mehouchi & Singh 2018; Rychert *et al.* 2020, 2021; Qin *et al.* 2020). For example, Mehouchi & Singh (2018) and Rychert *et al.* (2021) independently imaged plate thickness near the Mid-Atlantic Ridge that undulates in some locations.

Sublithospheric small-scale convection (SSC) is generally the preferred explanation of these oscillations on oceanic plates older than $\sim 70 \text{ Myr}$ (e.g. Parsons & McKenzie 1978; Fleitout & Yuen 1984; Buck & Parmentier 1986; Haxby & Weissel 1986; Stein & Stein 1992; Zlotnik *et al.* 2008; Ballmer *et al.* 2009, 2010; Likerman *et al.* 2021). SSC occurs when the cool base of the oceanic lithosphere drips off due to its negative buoyancy. The cold lithospheric mantle is replaced with hot asthenosphere, in a convective pattern called Richter Rolls (Richter 1973; Parsons & McKenzie 1978; Davaille & Jaupart 1994; Ritzwoller *et al.* 2004). Considerable work has been done to understand SSC in 2-D and 3-D, and its consequences for the thermal, mechanical and chemical evolution of the oceanic lithosphere (e.g. Richter 1973; Richter & Parsons 1975; van Hunen & Zhong 2006; Afonso *et al.* 2008; Zlotnik *et al.* 2008; Ballmer *et al.* 2010). Bull's-eye gravity anomalies (Tolstoy *et al.* 1993), more prevalent near slow-spreading ridges, may be evidence of SSC in the form of descending mantle diapirs.

However, the observed seismic velocity discontinuities cannot be explained using solely solid-state thermal variations invoked by previous work on SSC (Rychert *et al.* 2020). Seismic speeds are known to be sensitive to magma at grain boundaries (Blackman & Kendall 1997; Yang *et al.* 2007; Clark & Lesher 2017), grain size (Faul & Jackson 2005; Austin & Evans 2007; Gaherty *et al.* 1999), elastically accommodated grain boundary sliding (Karato 2012; Karato *et al.* 2015), near-solidus deformation (Yamauchi & Takei 2016), anisotropy (Auer *et al.* 2015; Beghein *et al.* 2014; Hansen *et al.* 2021), oxidation state of the mantle (Cline *et al.* 2018), bulk composition (Rader *et al.* 2015; Selway *et al.* 2015) and hydration

(Karato 2003; Faccenda *et al.* 2008). Of these, small amounts of melt (1–5.5%) could be the most straightforward explanation of the sharp change in seismic wave speed at the LAB (Abers *et al.* 2014; Selway & O'Donnell 2019; Qin *et al.* 2020; Rychert *et al.* 2021). Subplate partial melt, either intermittent or widespread, is consistent with intraplate volcanism and the petit-spot volcanoes observed on the outer rise in some subduction centres (Hirano *et al.* 2006; Pilet *et al.* 2016; Yang & Faccenda 2020).

1.3 Models of mantle flow

Several studies have tried to model the observed asymmetry in the MELT region by imposing asymmetric boundary conditions on a passive flow model (Conder *et al.* 2002; Toomey *et al.* 2002). In order to reproduce the observed asymmetry, these models require unrealistically large forcing, such as rapid asthenospheric cross-axis flow ($\sim 30 \text{ cm yr}^{-1}$) at high asthenospheric viscosities ($\sim 10^{21} \text{ Pa s}$), or temperature anomalies of more than 100 K beneath the East Pacific Rise (Conder *et al.* 2002; Toomey *et al.* 2002).

The observations outlined above suggest that mantle flow at MORs is more complicated than passive upwelling driven by plate spreading and conductive cooling of the lithosphere. In this study, we propose that buoyancy-driven flow may provide an explanation for both the asymmetric distribution of melt beneath the ridge axis and variations of the LAB. Buoyancy-driven flows are known to produce symmetry-breaking behaviour in fluid systems (e.g. Turner 1973); on Earth, chemical and thermal buoyancy are the main driving forces for mantle convection and plate tectonics (e.g. Coltice *et al.* 2019). At MORs, mantle melting creates additional sources of buoyancy via melt retention and/or depletion (Buck & Su 1989; Scott & Stevenson 1989; Parmentier & Phipps Morgan 1990; Jha *et al.* 1994; Harmon *et al.* 2011). This melt-induced buoyancy-driven flow may help explain observations of asthenospheric melt at a wide range of seafloor ages (Harmon *et al.* 2020). Buoyancy-driven flows are often referred to as active flows to differentiate from the passive flow case.

The dynamics of buoyancy-driven flow beneath MORs and oceanic lithosphere has often been investigated with single-phase flow models, without the treatment of melting. From the first computational study of local convection at MORs by Rabinowicz *et al.* (1984), which used a single-phase formulation and a parametrized effect of 5% retained porosity, single-phase numerical studies have gradually incorporated other sources of buoyancy, such as composition and temperature (e.g. Sotin & Parmentier 1989; Parmentier & Phipps Morgan 1990; Sparks & Parmentier 1993; Jha *et al.* 1994). Recent models have also added non-Newtonian viscosity (Ballmer *et al.* 2009), or three dimensions (Ballmer *et al.* 2010; Likerman *et al.* 2021). However, most of the previous computational work on SSC used a single-phase formulation with pure thermal instabilities (Ballmer *et al.* 2010; Likerman *et al.* 2021); this approach has helped to explain observations of variable LAB depths at older seafloor ages (Harmon *et al.* 2011, 2020).

The presence of partial melt was suggested to be a key factor for SSC to occur at both young and old seafloor age (Buck & Su 1989; Harmon *et al.* 2020). Moreover, SSC may promote additional partial melting of the asthenosphere. Thus, a second category of computational models have coupled mantle flow, melting and magmatic segregation with buoyancy (e.g. Buck & Su 1989; Scott & Stevenson 1989; Spiegelman 1993; Choblet & Parmentier 2001; Herlund *et al.* 2008; Ghods & Arkani-Hamed 2000).

These studies concluded that both porosity and chemical fractionation may cause buoyancy-driven flow in the mantle. However, they assumed cross-axis symmetry of flow and lacked a consistent coupling between the mechanics of two-phase flow and the transport of energy and composition in a multicomponent petrological system.

The current study builds on the model and results of Katz (2010), which also used a two-phase, two-component model for magma/mantle dynamics. That work considered convective mantle flow beneath the ridge axis driven by buoyancy associated with the presence of less-dense partial melt. In this context, Katz (2010) showed that a small, across-axis gradient of mantle potential temperature or composition is amplified to produce significant asymmetry in the distribution of upwelling and melting. This asymmetry increases with the vigour of buoyancy-driven mantle flow. However, Katz (2010) considered only the buoyancy associated with the residual porosity of the mantle matrix (porous buoyancy); it neglected variations in density due to temperature and composition.

Here, we investigate the role of compositional variation of density as an additional driver of flow beneath MORs. We present 2-D MOR models that incorporate density variations due to porosity and chemical differences arising from the Fe/Mg partitioning between melt and residue. Our models are based on consistent solutions of the equations governing magma dynamics from McKenzie (1984). They account for melting/freezing in a two-phase, two-component, energy-conserving, open petrological system in thermodynamic equilibrium (Katz 2022).

The manuscript is organised as follows. In Section 2, we describe our parametrization of buoyancy sources, review the governing equations, and provide a scaling analysis of convective flow. Section 3 presents results from numerical solutions on the contributions of compositional and porous buoyancy to convective upwelling and crustal production. This is followed by results on asymmetry and time-dependent flow forced by lateral temperature and compositional gradients. Finally, in Section 4, we discuss the implications of our results in the context of observations and previous work; we consider limitations of the model and how incorporating additional physics would modify our results.

2 METHODS

2.1 Sources of buoyancy in partially molten zones

During partial melting in the asthenosphere, density variations arise from thermal expansion, changes in chemical composition of the liquid and solid and dynamic retention of less dense magma within the pores of the mantle matrix. Here we neglect thermal effects on density as they are less likely to be important beneath the ridge axis, where the lithosphere is thin and melting and melt depletion are thought to dominate (Ito & Dunn 2009; Likerman *et al.* 2021).

2.1.1 Compositional density variations

Density variations due to composition are modelled using a linearized equation of state for each phase i (solid s or liquid ℓ),

$$\rho_i = \rho_{0i}(1 - \beta(C_i - C_0)), \quad (1)$$

where C_i is the concentration (by mass) of the less-dense component in phase i and β is the coefficient of compositional expansion. The constants $\rho_{0s} = \rho_0$, $\rho_{0\ell} = \rho_0 - \Delta\rho$ and C_0 are reference values

(Table 1). In eq. (1), the concentration C_i roughly corresponds to the magnesium number, $Mg\# = Mg^{2+}/(Mg^{2+} + Fe^{2+})$.

The partitioning of Fe and Mg between melt and mineral phases is considered to have the most significant chemical effect on density. At shallow asthenospheric depths, Fe-rich components partition preferentially into the melt, leaving a Mg-rich residue (higher $Mg\#$) with a reduced density. Changes in the modal proportion of dense minerals, such as spinel and/or garnet, can also affect density (Schutt & Leshner 2006); however, garnet is not a stable phase at low pressure and high temperature, and Fe/Mg partitioning alone can be used as an estimate of the density reduction due to melt extraction (Parmentier & Phipps Morgan 1990).

The effect of melt formation and segregation on density of the mantle residue has not been quantified definitively. Earlier studies suggested that for 25 % partial melting beneath MORs, the combined effects of Fe/Mg partition and dense-phase removal reduces the solid density by 1.9 % for garnet peridotite (Oxburgh & Parmentier 1977) and 1.4 % for fertile lherzolite (Scott & Stevenson 1989). Schutt & Leshner (2006) suggest that density changes following melt depletion in spinel peridotite might be significantly smaller, with only 0.42–0.46 % density decrease for 20 % melt extraction. However, melt depletion effects are dependent on pressure (Baker & Stolper 1994; Walter 1998; Schutt & Leshner 2006), initial bulk composition and melting path (Afonso & Schutt 2012; Pearson *et al.* 2021). Fractional melting experiments, which are more representative of the natural system, provide estimates for the change in density in fertile lherzolite of ~ 0.7 – 1.2 % for 20 % melting (Afonso & Schutt 2012; Pearson *et al.* 2021). To achieve a 1.2 % density change by thermal expansion requires a temperature change of 400 °C.

We constrain the expansivity parameter β in eq. (1) using the thermodynamics software pMELTS (Ghiorso *et al.* 2002; Ghiorso & Wolf 2019) via the ThermoEngine/ENKI software package. We solve for liquid and solid compositions during partial melting of fertile lherzolite compositions [i.e. MM3 (Baker & Stolper 1994), Appendix E]. We consider numerical melting experiments under isobaric, isothermal and isentropic conditions, for which we obtain average β values for the solid phase ranging between 0.50 and 0.78, with an overall average of 0.65. These values are similar to previously published studies; our percentage change of density due to chemical depletion is between 1.8 and 5.4 %, compared to 2.1 % in Schutt & Leshner (2006). Our thermodynamic calculations also show that both liquid and solid densities vary non-linearly with melt fraction and $Mg\#$ (Appendix E). For simplicity, we take β constant and equal among phases.

2.1.2 Bulk density of the two-phase aggregate

Bulk density $\bar{\rho}$ is a function of phase densities and the volume fraction of melt (porosity, ϕ),

$$\bar{\rho} = \phi\rho_{\ell} + (1 - \phi)\rho_s. \quad (2)$$

Since $\rho_{\ell} < \rho_s$ over the asthenospheric depths considered here, eq. (2) states that the bulk density is reduced at larger ϕ . The density difference between phases hence has two effects: it drives melt segregation through the permeable network of pores between mantle grains and it creates density variations of the two-phase aggregate that can drive convection. For 10 % porosity, bulk density is reduced by 1.7 %, which is equivalent to the effect produced by a temperature increase of 550 °C.

Table 1. Reference parameter values used in the scaling analysis and numerical simulations.

Parameter	Value	Comment
H	100	Height of domain [km]
L	200–1200	Length of domain [km]
U_0	2–6	Half-spreading rate [cm yr^{-1}]
g	9.8	Acceleration of gravity [m s^{-2}]
T_p	1648	Potential temperature of mantle [K]
c_P	1200	Specific heat of matrix and magma [$\text{J kg}^{-1} \text{K}^{-1}$]
\mathcal{L}	4×10^5	Latent heat [J kg^{-1}]
ρ_0	3000	Reference density of matrix and magma [kg m^{-3}]
$\Delta\rho$	500	Reference density difference [kg m^{-3}]
α	3×10^{-5}	Coefficient of thermal expansion [K^{-1}]
β	0–4	Coefficient of compositional expansion [(wt. frac.) $^{-1}$]
n	3	Exponent in porosity-permeability relationship [–]
K_0	10^{-8} – 10^{-6}	Permeability prefactor [m^2]
κ	10^{-6}	Thermal diffusivity [$\text{m}^2 \text{s}^{-1}$]
\mathcal{D}	10^{-8}	Chemical diffusivity [$\text{m}^2 \text{s}^{-1}$]
C_0	0.85	Reference composition [wt. frac.]
ΔC	0.10	Compositional difference between solidus and liquidus at T_0 [wt. frac.]
T_0	1565	Solidus temperature at $P = 0$, $C = C_0$ [K]
M	400	Slope of solidus and liquidus dT/dC [K]
γ^{-1}	60	Inverse Clapeyron slope dT/dP [K GPa^{-1}]
η_0	10^{18}	Reference matrix shear viscosity [Pa s]
ζ_0	4×10^{19}	Reference matrix compaction viscosity [Pa s]
ϕ_{\min}	10^{-6}	Minimum porosity for cutoff compaction viscosity [–]
$\eta_{\min/\max}$	$10^{15}/10^{25}$	Cut-off shear viscosity min/max [Pa s]
λ	27	Porosity weakening of shear viscosity
$\frac{E_A}{R}$	3.6×10^4	Activation energy divided by gas constant [K]
T_{η_0}	1672.82	Temperature at which viscosity is equal to η_0 [K]
μ	1	Magma viscosity [Pa s]
x_{MOR}	4	Distance from mid-ocean ridge axis for melt extraction [km]
f	0.2	Efficiency of melt extraction at the ridge axis [–]

2.2 Model description

The model builds on that of Katz (2010) and represents the numerical solution to a system of coupled equations representing conservation of mass, momentum, energy and composition for two phases (liquid and solid) and two components. The petrological model is based on a binary solid-solution phase diagram with fertile and refractory end-member components (Appendix A; Katz 2008, 2022; Katz & Weatherley 2012).

The conservation of mass and momentum of a two-phase system is based on the theory of McKenzie (1984),

$$\frac{\partial \rho_\ell \phi}{\partial t} + \nabla \cdot \rho_\ell \phi \mathbf{v}_\ell = \Gamma, \quad (3)$$

$$\frac{\partial \rho_s (1 - \phi)}{\partial t} + \nabla \cdot \rho_s (1 - \phi) \mathbf{v}_s = -\Gamma, \quad (4)$$

$$\phi(\mathbf{v}_\ell - \mathbf{v}_s) = -\frac{K}{\mu}(\nabla P_\ell - \rho_\ell \mathbf{g}), \quad (5)$$

$$\nabla P_\ell = \nabla \cdot \eta(\nabla \mathbf{v}_s + \nabla \mathbf{v}_s^T) + \nabla \left[\left(\zeta - \frac{2}{3} \eta \right) \nabla \cdot \mathbf{v}_s \right] + \bar{\rho} \mathbf{g}, \quad (6)$$

where \mathbf{v}_ℓ , \mathbf{v}_s are phase velocities, Γ is melting rate, P_ℓ is liquid pressure, η and ζ are the shear and compaction viscosity of the aggregate, respectively, K is permeability, μ is liquid viscosity and \mathbf{g} is the acceleration of gravity. We use a three-field pressure decomposition in which the liquid pressure is the sum of the lithostatic, the dynamic and the compaction pressures, $P_\ell = P_{\text{lith}} + P + \mathcal{P}$, to obtain the final system of equations for the mechanics (Katz *et al.* 2007; Keller *et al.* 2013, and Appendix A). Choosing a coordinate system with z increasing upward and $z = 0$ at the top of the domain we can write $\mathbf{g} = -g\mathbf{k}$ and lithostatic pressure $P_{\text{lith}} = -\rho_0 gz$.

For the thermochemical evolution of a two-phase, two-component system, the conservation of energy and composition can be written as

$$\frac{\partial \mathcal{H}}{\partial t} + \rho c_P e^{-\frac{\alpha g z}{c_P}} \nabla \cdot \bar{\mathbf{v}} T = \mathcal{L} \rho \nabla \cdot (1 - \phi) \mathbf{v}_s + k e^{-\frac{\alpha g z}{c_P}} \nabla^2 T, \quad (7)$$

$$\frac{\partial C}{\partial t} + \nabla \cdot \phi \mathbf{v}_\ell C_\ell + \nabla \cdot (1 - \phi) \mathbf{v}_s C_s = \mathcal{D} \nabla \cdot \phi \nabla C_\ell, \quad (8)$$

where \mathcal{H} is bulk enthalpy per unit volume, T is potential temperature, ρ is density, taken here as reference density of matrix and magma, c_P is specific heat capacity, α is the coefficient of thermal expansion, $\bar{\mathbf{v}}$ is bulk velocity, C is bulk composition, \mathcal{L} is specific latent heat, k is thermal conductivity and \mathcal{D} is chemical diffusivity. Thermal expansivity, previously neglected in the density model, is included here in the potential temperature formulation. Closure conditions for the energy and composition equations are provided by a two-component phase diagram and the Enthalpy method (Alexiades & Solomon 1993), which assumes thermodynamic equilibrium. This method determines potential temperature, phase compositions and porosity given \mathcal{H} , C and P_{lith} (Katz 2008, 2010; Katz & Weatherley 2012, and Appendix A).

Constitutive equations for shear and compaction viscosity, which are temperature- and porosity-dependent after Hirth & Kohlstedt (2003) and Karato & Wu (1993), are given by

$$\eta = \eta_0 \exp \left[\frac{E_A}{R} \left(\frac{1}{T} - \frac{1}{T_{\eta_0}} \right) - \lambda \phi \right], \quad (9)$$

$$\zeta = \zeta_0 \exp \left[\frac{E_A}{R} \left(\frac{1}{T} - \frac{1}{T_{\eta_0}} \right) \right] \phi^{-1}, \quad (10)$$

where E_A is activation energy, R is the universal gas constant, λ is a positive constant and ζ_0 and η_0 are reference compaction and

shear viscosities. T_{n0} is a reference temperature chosen such that the viscosities assume their reference values at a depth just beneath the onset of partial melting. In eq. (10), compaction viscosity is proportional to $1/\phi$, the dependency expected if both the solid and liquid are treated as Newtonian viscous fluids at the grain scale (e.g. Hewitt & Fowler 2008; Simpson *et al.* 2010). In contrast, Rudge (2018a) modelled diffusion of vacancies at grain scale and found a compaction viscosity proportional to the log of porosity for Nabarro–Herring creep and proportional to the shear viscosity for Coble creep. The leading effect of these differences is on the predicted compaction length at reference parameters (Katz *et al.* 2022).

Permeability is calculated according to the Kozeny–Carman relationship (Wark & Watson 1998; Wark 2003; Rudge 2018b) in the limit of small ϕ ,

$$K = K_0 \phi^n, \quad (11)$$

where K_0 is the permeability prefactor and n is permeability exponent. Parameter values are given in Table 1 and more details on the full system of equations and non-dimensionalization are provided in Appendix A.

2.2.1 Model domain, initial and boundary conditions

We run models with two domain configurations: (1) half-ridge models to investigate the convective vigour and (2) full-ridge models to investigate development of asymmetry and time-dependent flow. In both cases, the domain is 2-D, rectangular and normal to the ridge axis. We explain the difference below.

The domain and boundary conditions for half-ridge models are shown in Fig. 1. The ridge axis is located on the left boundary; we model the dynamics of melt and mantle flow beneath one oceanic plate. The height of the domain is 100 km, while the half-width varies among simulations between 200 and 600 km. Wider domains are used to avoid melting due to buoyancy-driven flow at the domain boundaries. Symmetry is imposed across the ridge axis by the application of reflection boundary conditions; zero horizontal component of the solid velocity prevents flow through the left boundary. The bottom and right boundaries use inflow/outflow conditions to allow material enter the domain from below and leave the domain laterally. The top boundary has a specified solid velocity $\mathbf{v}_s = [U_0, 0]$, where U_0 is the half-spreading rate. The bottom boundary has fixed enthalpy H_p , corresponding to the mantle potential temperature at zero porosity. Away from the ridge (distance $|x| > x_{\text{MOR}}$), the top boundary has a fixed enthalpy H_C , corresponding to a surface temperature of 0 °C.

Melt is allowed to escape the domain within a small distance from the ridge axis ($|x| \leq x_{\text{MOR}}$). In previous work, melt extraction at the axis has been modelled in various ways: through a vertical ‘dike’ at the ridge axis (Katz 2010), a horizontal window on top of domain (Sim *et al.* 2020) or through an imposed patch that extends vertically and horizontally (Keller *et al.* 2017). Our approach most closely resembles the horizontal window at the top of the domain, but differs slightly from previous work. We first set enthalpy boundary conditions $\partial H/\partial z = 0$ for $|x| \leq x_{\text{MOR}}$. Within the melt-extraction window at the top of the domain, we impose a reduced permeability $K_{\text{top}} = K_0(f\phi)^n$, where $f < 1$ is an extraction efficiency parameter (Table 1, Appendix C). A value of f between 0.1 and 0.2 yields crustal thicknesses of 5–12 km, comparable to recorded oceanic crustal thicknesses (White *et al.* 2001).

In full-ridge simulations, the domain extends to both sides of the ridge axis to capture the full width of the melting region (i.e. width of $2L$). The boundary conditions on the left-hand side of domain now become outflow boundary conditions, while imposed plate divergence on the top boundary is symmetrical across the axis.

The conservation of energy and composition equations require initial conditions. We follow the approach of Ghods & Arkani-Hamed (2000) and Katz (2008, 2010) to construct these. The composition field is initialized with a uniform bulk composition C_0 and the enthalpy field according to the sensible heat content associated with a half-space cooling model

$$T(x, z) = T_0 + (T_m - T_0) \text{erf}\left(\frac{z}{2\sqrt{\kappa t}}\right), \quad (12)$$

$$\mathcal{H}(x, z) = \rho c_P [T(x, z) - T_0], \quad (13)$$

where T_0 is surface temperature, $T_m = T_{\text{exp}}(\alpha g H / c_P)$ is mantle temperature corresponding to potential temperature at depth H of the bottom of domain and $t = x/U_0$ is plate age. The initial enthalpy $\mathcal{H}(x, z)$ is then reduced by the amount that is contained in latent heat, $\rho \mathcal{L} \phi(x, z)$; the initial bulk composition is updated to be equal to the computed C_s . Together these yield an equilibrium porosity that is zero everywhere in the domain.

The governing equations are discretized using finite differences on a staggered grid, and solutions are obtained in a new software layer called FD-PDE (Appendix C) that augments the Portable, Extensible Toolkit for Scientific Computation (PETSc, Balay *et al.* 2019). The simulations are run at resolution of 1 km per grid cell for 3–5 Myr until they reach a state in which crustal production and distribution of partial melt are roughly constant (i.e. convergence for crustal thickness is below tolerance, $dh_{\text{crust}}/dt < 10^{-4} \text{ m yr}^{-1}$). Predicted crustal thickness is calculated as the ratio of the rate at which melt volume crosses the window and leaves the domain to the plate spreading rate (Keller *et al.* 2017). Simulations with slow spreading rate ($U_0 = 2 \text{ cm yr}^{-1}$) produce long-term, periodic oscillation of crustal thickness. In this case, steady-state values are defined as the average between 4 and 5 Myr. Some simulations displaying time-dependent flow were run for 10–13 Myr.

2.3 Scaling analysis

Convection is typically studied in terms of the Rayleigh number, which is the dimensionless ratio of factors driving convection to those resisting it (e.g. Turcotte & Schubert 2014). A parameter similar to the Rayleigh number for porous buoyancy beneath a MOR was derived by Spiegelman (1993) and Katz (2010). Here, we extend the scaling analysis to account for compositional buoyancy beneath a MOR.

We assume that the viscosity is constant, $\eta = \eta_0$, a simplification applied only in this section to establish a basic understanding of dynamics. We then take the curl of eq. (6), non-dimensionalize and group terms (details in Appendix D) to obtain a vorticity equation

$$\nabla^2 \omega = \nu_\phi \partial_x \phi + \nu_C \partial_x F, \quad (14)$$

where $\omega \hat{\mathbf{j}} = \nabla \times \mathbf{v}_s$ is vorticity, ∂_x is a partial derivative with respect to x and $F = (C_s - C_0)/\Delta C$ is the degree of melting (a dimensionless measure of solid depletion). The vorticity equation states that lateral gradients in porosity and composition are an internal source of vorticity. Two dimensionless buoyancy numbers are used in eq. (14), ν_ϕ and ν_C . Because steady-state depletion is constant along the horizontal streamlines in the lithosphere, $\partial_x F \sim 0$ and we focus on

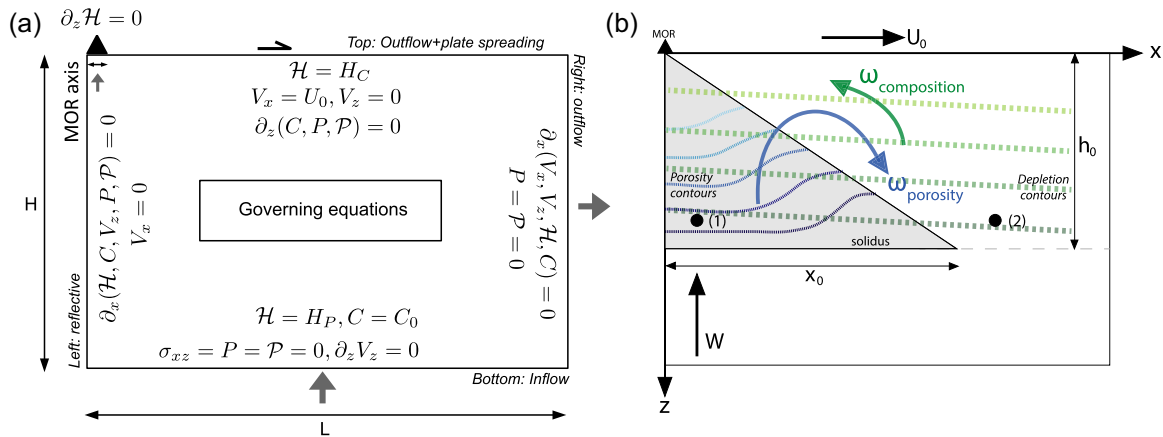


Figure 1. (a) Numerical model setup and boundary conditions for a half-ridge domain. The left boundary has reflection boundary conditions, the bottom boundary has inflow conditions, the right boundary has outflow conditions, and the top boundary has the imposed half-spreading rate and surface temperature. Parameters: \mathcal{H} is enthalpy, C is bulk composition, P is dynamic pressure, \mathcal{P} is compaction pressure, V_x, V_z are horizontal and vertical components of solid velocity \mathbf{v}_s , ∂_x represents the partial derivative w.r.t. x , H_C is enthalpy at surface temperature, H_P is enthalpy corresponding to potential mantle temperature at the bottom of domain, C_0 is reference composition, L is domain length and H is domain height. (b) Schematic of porosity and degree of melting F contours in a steady-state half-ridge model. Both porosity and depletion increase at shallower depths. Vorticity due to porous buoyancy enhances upwelling beneath the axis and induces some downwelling off axis; this creates a small lateral gradient in depletion. Acting on this gradient, compositional buoyancy has a counterbalancing effect. The buoyancy force in the system can be estimated using the lateral density difference between points 1 and 2.

v_ϕ , which is

$$v_\phi = \frac{gh_0^2}{\eta_0 U_0} \left(\frac{\mu W_0 F_0}{K_0 \Delta \rho g} \right)^{1/3} [\Delta \rho - \beta \Delta C (\rho_0 - \Delta \rho + F_0 \Delta \rho)], \quad (15)$$

where h_0 is the maximum height of melting column, W_0 is passive mantle upwelling rate, F_0 is degree of melting at top of the column, U_0 is half-spreading rate and $\Delta \rho$ and ΔC are density and compositional phase differences. Parameter values are given in Table 1.

In the case of $\beta = 0$, where the phase densities are independent of composition, $v_C = 0$ and v_ϕ reduces to that defined in Spiegelman (1993). Eq. (15) shows that when $\beta > 0$, the compositional effect on vorticity is negative—counter to that of porosity. Chemical depletion of the residue with progressive melting establishes a stabilising (anti-convective) density stratification, as illustrated in Fig. 1(b). For parameters as in Table 1, the net effect of porous and compositional buoyancy remains positive as long as $\beta < 1.9$. Hence we expect that compositional density variations incompletely suppress the buoyancy-driven upwelling associated with partial melting.

Katz (2010) showed that v_ϕ can be used to obtain a quantitative prediction of the maximum subridge upwelling rate relative to that of passive flow. If $\partial_x F \sim 0$, the fit to simulations obtained by Katz (2010) should hold for our results with non-zero β . Fig. 4 shows that this is indeed the case.

3 RESULTS

Results are presented in three subsections that investigate: (1) vigour of buoyancy-driven upwelling relative to passive flow using half-ridge models, (2) across-axis asymmetry of upwelling and melting in steady-state, full-ridge models and (3) time-dependent, SSC in full-ridge models. Parameters values are as in Table 1 unless otherwise stated.

3.1 Role of buoyancy in half-ridge models

Half-ridge models are run to investigate the vigour of upwelling due to buoyancy forces. We compare the results to the scaling analysis in

Section 2.3. First, we present model outcomes that compare passive flow with two cases of active flow. Passive flow is that arising when $\bar{\rho}\mathbf{g}$ is excluded from the momentum eq. (6); mantle flow is driven only by plate divergence. Active flow is when $\bar{\rho}\mathbf{g}$ is included such that buoyancy-driven mantle flow can occur. When $\beta = 0$, active flow is due to porous buoyancy only; when $\beta > 0$ both porous and compositional buoyancy play a role in determining the flow. We consider a range of β values so as to measure the sensitivity and phenomenology arising from compositional buoyancy.

Fig. 2 shows output from these three flow cases, after simulations have reached steady-state. Column A shows passive flow; column B shows active flow with porous buoyancy ($\beta = 0$); and column C shows active flow with porous and compositional buoyancy ($\beta = 1$). Other parameters are the same among these simulations—the only difference between them is how the body-force term is treated. Models in columns A and B reproduce results in (Katz 2010).

The top row of panels in Fig. 2 are porosity maps with temperature contours and solid-velocity streamlines. The middle row shows maps of $\bar{\rho} - \rho_0$, the difference between the bulk density and the solid density of the unmolten mantle; vectors represent the liquid velocity. The bottom row of panels show the vertical component of solid velocity. The boundary of the partial-melt zone is marked by a continuous black line in all panels. Simulations presented here have compaction length on the order of 10 km, which suppresses formation of porosity waves and enhances melt focusing to the ridge axis (Keller et al. 2017).

Comparing the mantle streamlines between the three columns of Fig. 2 shows that the mantle flow patterns for passive and active flow share broadly similar features. However, the upwelling rate (panels c, f and i) reveals that active flow has faster upwelling within the partial-melt zone, and downwelling at the lateral edge of the melting region. The magnitude of this convective perturbation is highest when only porous buoyancy is considered (panel f). Consistent with the scaling analysis, this effect is diminished by non-zero β (panel i).

Fig. 3 shows results from simulations in which two other, non-zero values of β are applied. All other parameters are the same as in

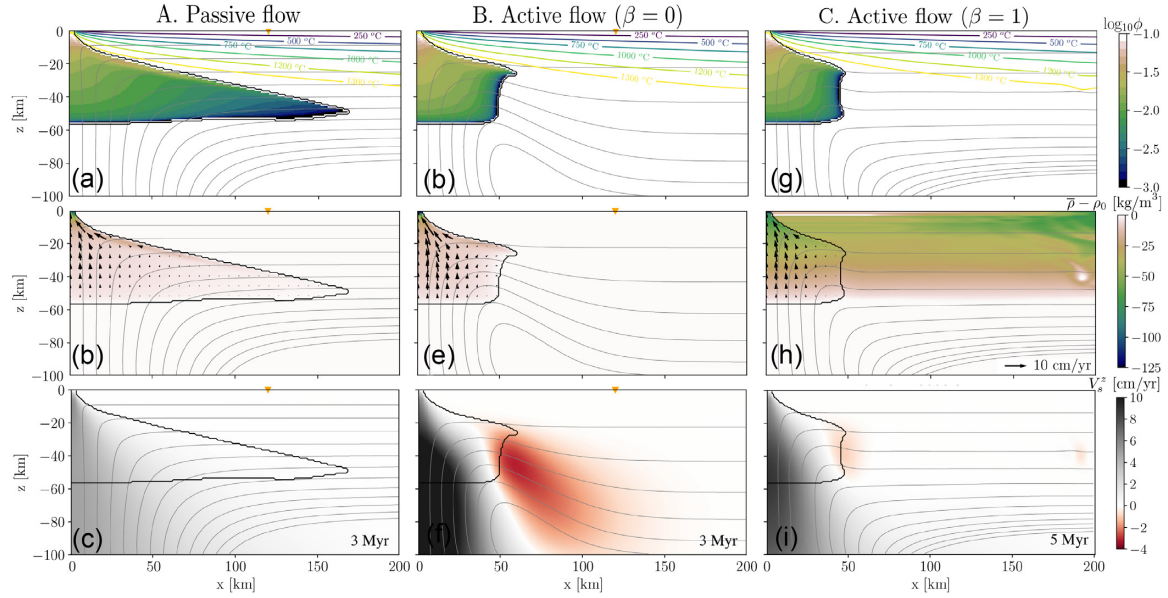


Figure 2. Model results for three representative cases: A. Passive flow, B. Active flow (porous buoyancy) and C. Active flow (porous and compositional buoyancy). All results are steady state, as defined in the main text. Results obtained with half-spreading rate $U_0 = 4 \text{ cm yr}^{-1}$, reference viscosities $\zeta_0 = 4 \times 10^{19} \text{ Pa s}$ and $\eta_0 = 10^{18} \text{ Pa s}$, permeability constant $K_0 = 10^{-8} \text{ m}^2$ and other parameters as given in Table 1. Colour maps are porosity (top row), bulk density relative to unmolten mantle density (middle row), and vertical component of solid velocity (bottom row). Grey lines are streamlines of the solid; black contour is the outline of the partially molten region; temperature contours are shown in colour in top panels; orange triangles indicate plate-spreading distance from the ridge axis. Resolution is 1 km (200 km \times 100 km domain in A and B, 600 \times 100 km domain in C).

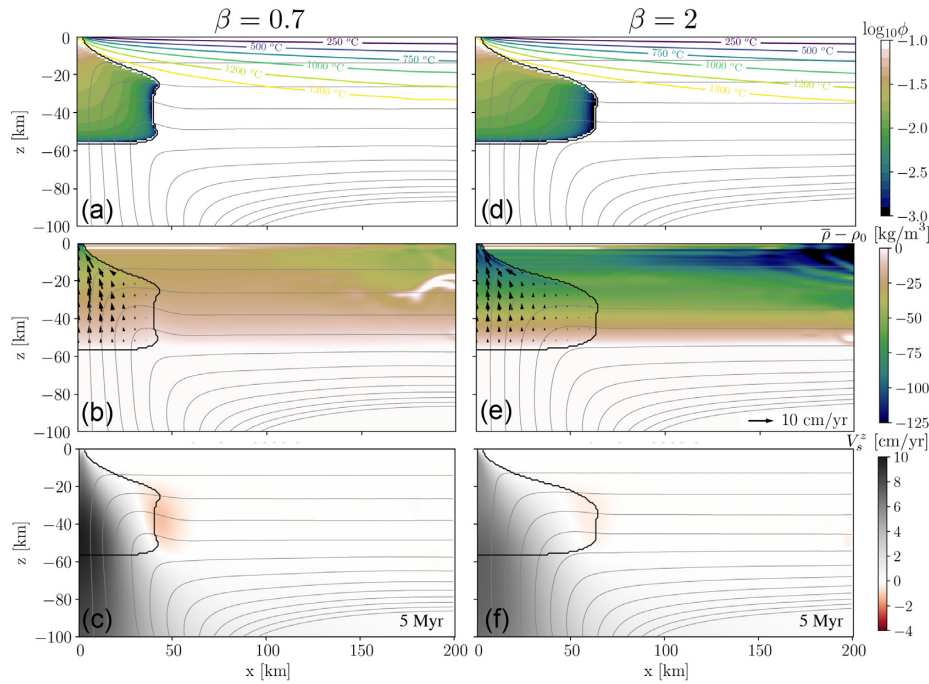


Figure 3. Steady-state results for low and high values of β in active flow models (porous and compositional buoyancy). All other parameters as in Fig. 2C. Domain size is 600 km \times 100 km with a resolution of 1 km.

Fig. 2. The leading effect of β is on the magnitude of bulk density difference between the unmolten mantle and the depleted residue forming the lithosphere (panels b and e). For $\beta = 0.7$ the relative density variations are within 50 kg m^{-3} , or less than 1.6% density change, while larger β values give higher density contrasts. When $\beta = 2$, panel (e) shows a strong density stratification in the partial-melt zone and lithosphere due to melting and melt extraction. The

width of the melting region increases for larger β , making its shape tend towards that obtained under passive flow. Note that our best estimate for β in the natural system is about 0.65.

It is evident from numerical solutions presented so far that the rate of upwelling decreases with increasing β . We quantify this trend by considering the ratio W_{max}/W_0 , where W_{max} is maximum upwelling rate within the simulated domain and W_0 is maximum

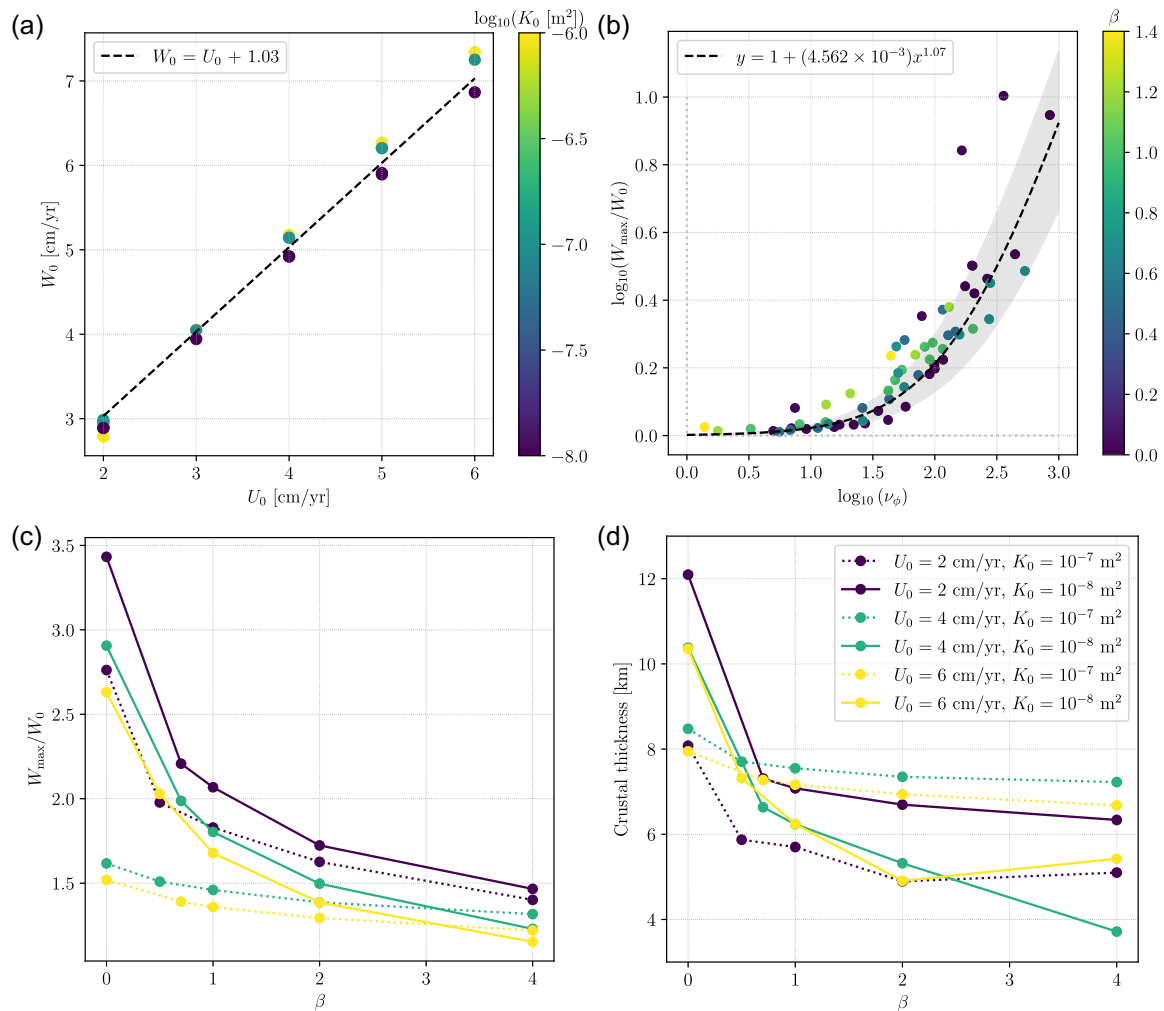


Figure 4. (a) Linear fit between maximum upwelling speed W_0 and half-spreading rate U_0 in passive flow models. (b) Scaling of maximum upwelling with effective porous buoyancy number as in eq. (15). Black dotted line is fitted curve from Katz (2010) and shaded areas are 95 % confidence intervals associated with the fit. Each point represents a simulation result taken at steady-state, as defined in the text. Parameter variations include half-spreading rates U_0 of 2, 3, 4, 5 and 6 cm yr^{-1} , shear viscosity prefactor η_0 ranging between 5×10^{17} and 10^{19} Pa s, the permeability prefactor K_0 ranging between 10^{-8} and 10^{-6} m^2 , and coefficient of chemical expansion β ranging between 0 and 1.4. (c) Maximum upwelling and (d) crustal thickness versus β for slow ($U_0 = 2 \text{ cm yr}^{-1}$), intermediate ($U_0 = 4 \text{ cm yr}^{-1}$) and fast ($U_0 = 6 \text{ cm yr}^{-1}$) half-spreading rates. Panel (c) shares the legend shown in panel (d). Cases of porous buoyancy are represented by $\beta = 0$, while non-zero values represent cases of porous-compositional buoyancy.

upwelling rate for passive flow at otherwise identical conditions. We refer to the quantity W_{max}/W_0 as the convective vigour. The passive upwelling rate W_0 varies linearly with the half-spreading rate U_0 . Previous work obtained $W_0 \sim 1.4U_0$ (Katz 2010). We find a different scaling, shown in Fig. 4(a), with $W_0 = U_0 + 1.03$ as a best fit to normalize our numerical results relative to passive flow case. This scaling obviously does not hold as $U_0 \rightarrow 0$.

Using this relationship, we investigate the effect of β on convective vigour while keeping all other parameters constant. Fig. 4(c) shows that increasing β decreases W_{max}/W_0 for slow, intermediate and fast spreading rates, and for different values of permeability prefactor K_0 . Enhanced upwelling should lead to enhanced melting and hence thicker crust. Fig. 4(d) confirms this. It also shows that predicted crustal thickness remains roughly constant for $\beta > 0.5$ for the same set of parameters.

The porous buoyancy number ν_ϕ can be used to predict the rate of upwelling in MOR models where thermal and compositional density variations are neglected (i.e. for $\beta = 0$, Katz 2010). We extend this

to $\beta > 0$ and quantify the relationship between convective vigour W_{max}/W_0 and the updated form of the porous buoyancy number ν_ϕ (eq. 15) that is a function of β .

Fig. 4(b) shows steady-state data from a suite of simulations with porous and compositional buoyancy. The coloured points represent model results over a range of half-spreading rates, viscosity prefactors η_0 , permeability prefactors K_0 and other parameter variations as given in figure caption. From each simulation, we extract height of melting column h_0 and reference degree of melting F_0 at steady-state in order to calculate the buoyancy number ν_ϕ . Values on the y-axis greater than zero represent cases where buoyancy-driven flow enhances the rate of mantle upwelling. The dotted black line in Fig. 4(b) is the curve $y = 1 + a\nu_\phi^b$, with a, b values as obtained by Katz (2010) for simulations with porous buoyancy only. Our results with porous and compositional buoyancy are consistent with this fit for different β , albeit with increased scatter.

The correlation between ν_ϕ and convective vigour in Fig. 4(b) confirms that porous buoyancy is the dominant cause of active

flow, and that there is an offsetting contribution from compositional buoyancy. In short, porous buoyancy promotes convective upwelling beneath the ridge while compositional buoyancy suppresses it. Results from simulations on domains that span the entire ridge axis, presented below, show that compositional buoyancy has additional effects on the dynamics of the system.

3.2 Asymmetry in steady-state, full-ridge models

Half-ridge simulations force symmetry across the ridge axis by the choice of boundary conditions. In this section, we consider a 2-D full-ridge domain with the ridge axis in the middle, at $x = 0$. A constant gradient in temperature or composition is imposed along the bottom (inflow) boundary to force asymmetry (Katz 2010). We investigate how buoyancy-driven flow amplifies this asymmetry relative to passive flow. In some cases, the forcing combined with buoyancy leads to time dependence of the flow. In this section, we consider only models that achieve a steady-state. All full-ridge results were obtained with reference parameters $\eta_0 = 10^{18}$ Pa s, $\zeta_0 = 4 \times 10^{19}$ Pa s and $K_0 = 10^{-7}$ m².

We quantify the degree of asymmetry using the metric defined by Katz (2010),

$$\Psi = 2 \frac{\int_{\Omega_+} S_\phi dA}{\int_{\Omega} S_\phi dA} - 1, \quad (16)$$

where $S_\phi(x, z) = 1$ if $\phi(x, z) > 0$ and is otherwise zero. Ω is the entire domain; Ω_+ is the half of the domain at $x > 0$. When $\Psi = 1$, all of the porosity is found to the right-hand side of the ridge axis, $\Psi = 0$ when porosity is distributed evenly across the axis and $\Psi = -1$ when all the porosity is on the left-hand side.

Fig. 5 shows simulation results in which a temperature gradient of 0.03 K km^{-1} is imposed on the bottom boundary. Panels compare passive and active flow cases for intermediate half-spreading rate $U_0 = 4 \text{ cm yr}^{-1}$. The imposed thermal gradient gives a temperature difference of 12 K from the left-hand side ($x = -200 \text{ km}$) to the right-hand side ($x = 200 \text{ km}$) of the domain in each of the models. Under passive flow, this forcing leads to a porosity asymmetry of only 4%. When buoyancy also drives flow, the forcing asymmetry is amplified. In panel (b), with $\beta = 0$, the degree of asymmetry is almost double the passive flow case. Enhanced melting on the slightly warmer right-hand side of the domain leads to more melting and more porous buoyancy there. To produce asymmetry of $\sim 10\%$ under passive flow requires a thermal forcing of 0.1 K km^{-1} , or about 40 K across the domain. Katz (2010) showed that for porous buoyancy only ($\beta = 0$), thermal forcing $\partial_x T$ of 0.03 to 0.18 K km^{-1} leads to even greater asymmetry.

Panels c and d of Fig. 5 show results for $\beta > 0$. At $\beta = 0.5$ there is a 23 % asymmetry of porosity while for $\beta = 2$ the asymmetry is greater than 35%. Evidently, although compositional buoyancy suppresses convection in half-ridge models, it promotes asymmetry of upwelling under active flow. This can be understood in terms of melting and melt segregation. Enhanced melting and efficient segregation on the warmer side of the ridge axis leads to greater depletion of the residue, lower bulk density and positive buoyancy relative to the cooler side of the ridge. This promotes enhanced upwelling on the warmer side, which feeds back to reinforce the buoyancy difference.

Fig. 6 shows results for models with chemical forcing, for the same reference parameters as in the case with thermal forcing. A lateral gradient of bulk composition of $\partial_x C$ of 10^{-6} (wt. frac.) km^{-1} is imposed on the bottom boundary, making the left-hand side more

fertile and the right-hand side more refractory. To put this into context, 20 % melting over a column height of 60 km beneath the ridge axis creates a gradient $\partial_z C \sim 10^{-4}$ (wt. frac.) km^{-1} , two orders of magnitude larger than the forcing.

In the compositionally forced, passive-flow case (Fig. 6a), the fertile mantle to the left of the axis enhances melting and porosity to the left; the degree of asymmetry is less than 0.1 percent and negative. Porous buoyancy (Fig. 6b) amplifies this effect by promoting upwelling and further melting on the left of the ridge axis.

Cases of active flow with compositional buoyancy develop a much higher degree of asymmetry compared to cases with porous buoyancy only. In Fig. 6, asymmetry varies from -0.2% for $\beta = 0$ to 9% for $\beta = 0.5$ and 16% for $\beta = 2$. Asymmetry also changes sign for cases with compositional buoyancy. With $\beta > 0$, the unmolten, fertile mantle to the left of the axis is negatively buoyant and the refractory mantle at right is positively buoyant. Therefore, the more refractory mantle to the right of the axis will tend to preferentially rise, driving excess melt generation and larger porosity. This asymmetry is positive and increases with β . Mantle streamlines in cases of compositional buoyancy (Figs 6c and d) deviate from the symmetrical corner-flow pattern, reflecting the solid mantle buoyancy at depth.

Fig. 7 shows the degree of asymmetry Ψ as a function of β for thermal forcing in panel (a) and chemical forcing in panel (b). Under thermal forcing, both porous and compositional buoyancy amplify the asymmetry in the system. Results with $\beta > 0$ develop higher asymmetry compared to results with porous buoyancy only ($\beta = 0$) for the same magnitude of forcing. Alternatively, smaller forcing is required to obtain same degree of asymmetry in models with compositional buoyancy, compared to porous-buoyancy-only models (e.g. 7 % asymmetry is obtained for 0.01 K km^{-1} forcing and $\beta = 0.5$, or 0.03 K km^{-1} and $\beta = 0$). Fig. 7(b) shows that small chemical forcing that barely perturbs the $\beta = 0$ case can induce notable asymmetry for $\beta > 0$.

Fig. 7(c) shows the effect of spreading rate on asymmetry in simulations with compositional buoyancy, while holding $\beta = 2$. For this set of experiments, we choose a larger value of β because we expect a greater sensitivity to other parameters. However, results show that asymmetry increases only modestly with increasing half-spreading rate.

3.3 Time-dependent active flow in full-ridge models

In this section we consider combinations of $\beta > 0$ and mantle forcing that do not give rise to a steady-state mantle flow. Instead, a larger forcing leads to the development of convective instabilities, delamination of the lower lithosphere and time-dependent convective flow. Fig. 8 shows snapshots of unsteady model results with a lateral temperature gradient of 0.05 K km^{-1} (panel a), and composition gradient of 5×10^{-6} (wt. frac.) km^{-1} (panel b) on the bottom boundary. Colourmaps represent bulk density relative to the reference, unmolten mantle density.

Under thermal forcing, instabilities are driven by melt pooling and crystallization at the lithosphere–asthenosphere boundary, which causes small-scale time-dependent flow (Fig. 8a). The high degree of asymmetry ($\sim 50\%$) induced by this forcing hinders melt focusing towards the ridge axis; melt further away from the axis is trapped in localised pools below the lithosphere. With plate cooling, melt pools crystallize into a solid that is more fertile and hence denser than the underlying, refractory residue. This creates an

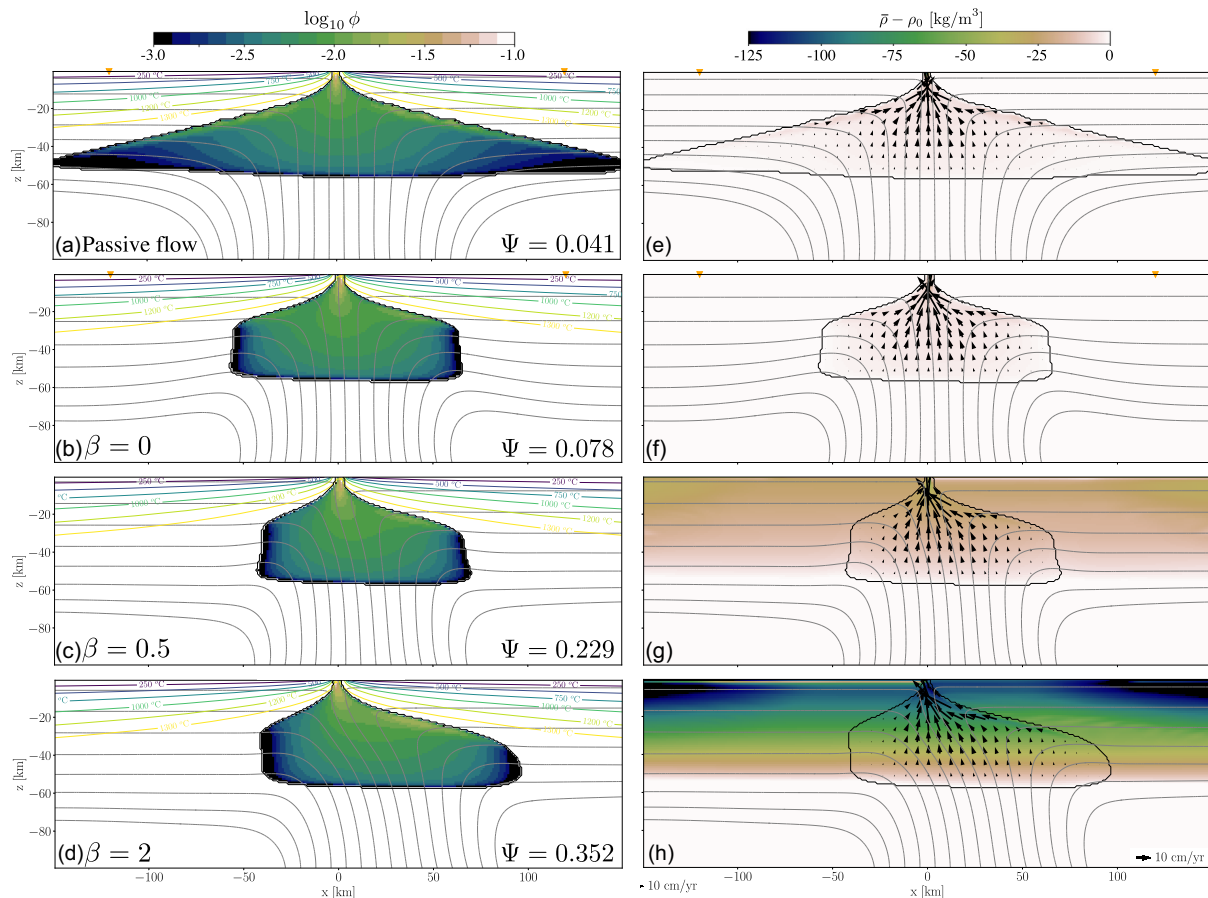


Figure 5. Full-ridge model results with temperature forcing on the bottom boundary $\partial_x T = 0.03 \text{ K km}^{-1}$ and intermediate half-spreading rate $U_0 = 4 \text{ cm yr}^{-1}$. Left-hand column shows porosity maps with temperature contours and mantle streamlines, while right-hand column shows relative bulk density maps with mantle streamlines and liquid velocity arrows. Ψ represents the degree of asymmetry of the partial-melt zone.

instability where chemically denser material sinks back into the asthenosphere, as seen in Fig. 8(a) at ~ 80 – 200 km distance from the axis. The lithospheric delaminations lead to undulations in temperature contours (see Movies S1 and S2).

Increased forcing leads to time-dependent flow affecting the entire melting region, as shown in Fig. 8(b) for a case with chemical forcing. Asymmetry changes drastically over time (changing sign from -10 to 55%). Model results at 9 Myr show a narrow distribution of melt beneath the axis and low degree of asymmetry. By 10.5 Myr , partial melting is widely distributed and with a high degree of asymmetry. Multiple isolated melt regions may exist at one time beneath the ridge axis. This affects melt transport and focusing, as shown by the black liquid velocity arrows in Fig. 8(b).

Lithospheric drips form preferentially at the lithosphere–asthenosphere boundary, causing large chemical heterogeneities to the right of the axis. However, the system is convecting vigorously such that drips may also be transported beneath the ridge axis. This transport and the complex pattern of compositional heterogeneity can suppress melting or enhance it, depending on the composition of the advected material. Furthermore, active flow may cause melt production further away from the axis, even at distances $>200 \text{ km}$. This type of convective flow also leads to undulations in lithospheric isotherms (see Movies S3 and S4).

Fig. 9 maps out the conditions under which we obtain time-dependent results. Model outcomes are shown for different thermal

(panel a) and chemical (panel b) forcing and a range of β . All cases with only porous buoyancy $\beta = 0$ resulted in a steady-state flow. Time-dependent flow occurs at larger forcing and β values. With a more compositional buoyancy, melt segregation creates larger density differences and the system becomes more sensitive to external forcing.

4 DISCUSSION

We presented results of MOR models that incorporate density variations due to the low density of the liquid relative to the solid (porous buoyancy), and the Fe/Mg partitioning between melt and its residue (compositional buoyancy). The refractory solid residue mantle produced in the melting region moves laterally with time, leading to a horizontal layer of lower density in the lithosphere and asthenosphere (Sotin & Parmentier 1989; Raddick *et al.* 2002). This constitutes a stable density stratification, which suppresses upwelling driven by porous buoyancy in half-ridge models (Fig. 1b). The scaling analysis in Section 3.1 quantifies how the vigour of upwelling is a function of porous buoyancy, which enhances convective upwelling, and compositional buoyancy (β), which suppresses it.

Full-ridge models with thermal and chemical forcing show, instead, that cross-ridge asymmetry is enhanced when $\beta > 0$ (Figs. 5

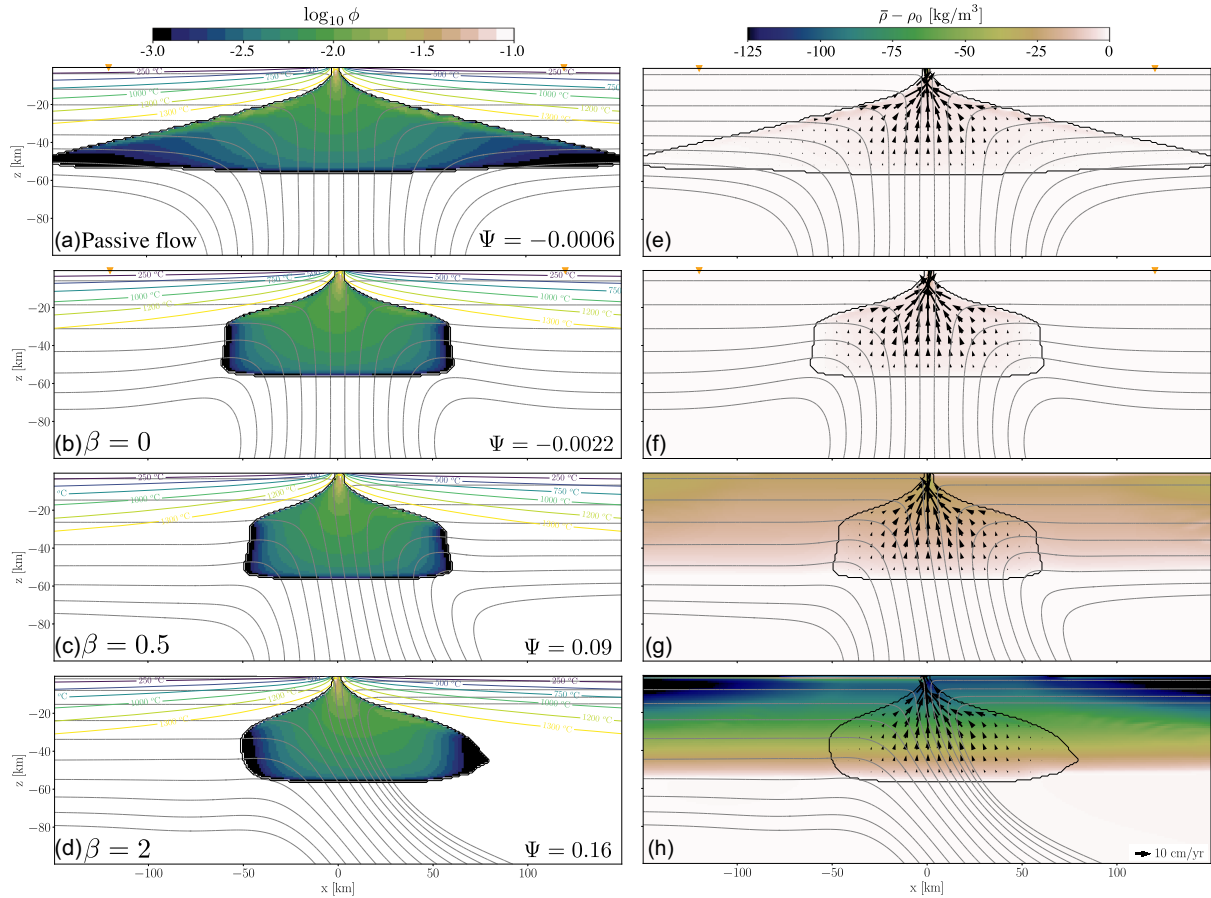


Figure 6. Full-ridge model results with chemical forcing on the bottom boundary $\partial_x C = 10^{-6}$ (wt. frac.) km^{-1} . Maps and parameters same as in Fig. 5. Asymmetry is negative in passive flow and porous-buoyancy flow cases, and changes sign with increasing compositional buoyancy. Asymmetry also develops more readily for compositional buoyancy cases, with more deflected streamlines.

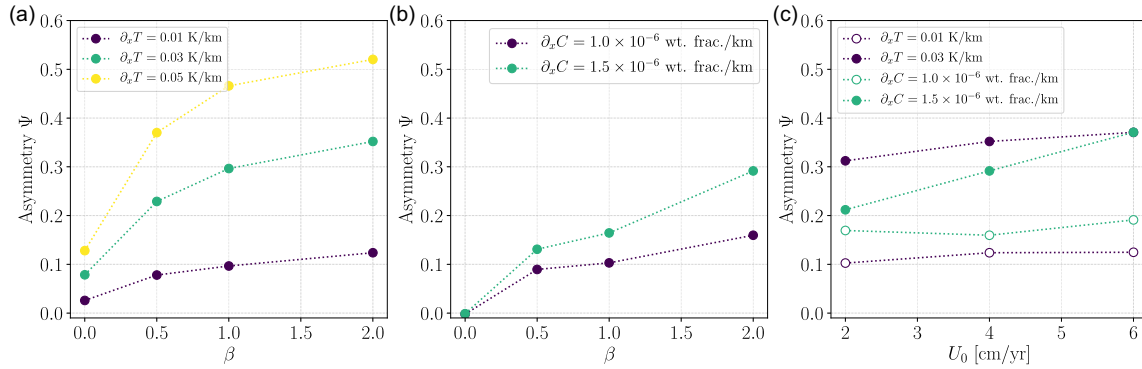


Figure 7. Asymmetry parameter versus β for temperature (a) and chemical (b) forcing of the system and $U_0 = 4 \text{ cm yr}^{-1}$. Each point represents a full-ridge model result that reached steady-state. Coloured lines represent different thermal and chemical forcing. (c) Asymmetry parameter versus spreading rate for temperature and chemical forcing of the system with $\beta = 2$.

and 6). With increased forcing and compositional buoyancy, models predict time-dependent, sublithospheric delamination and convection, with varying degrees of asymmetry in the distribution of partial-melt (Fig. 8).

This work extends a hypothesis to explain the asymmetry in magmatism across the axis of some MORs (Katz 2008; Melt Seismic Team 1998; Rychert *et al.* 2020). MOR models invoking passive flow require unrealistically large forcing to explain this asymmetry

(Conder *et al.* 2002; Toomey *et al.* 2002). In contrast, Katz (2010) found that models with porous buoyancy-driven flow may develop significant asymmetry with only modest forcing. Forcing in that work (and in the present manuscript) refers to long-wavelength mantle heterogeneity.

Building on the results of Katz (2010), we find that density variations associated with Fe/Mg fractionation further amplify the effects of pre-existing mantle heterogeneity. Compositional density

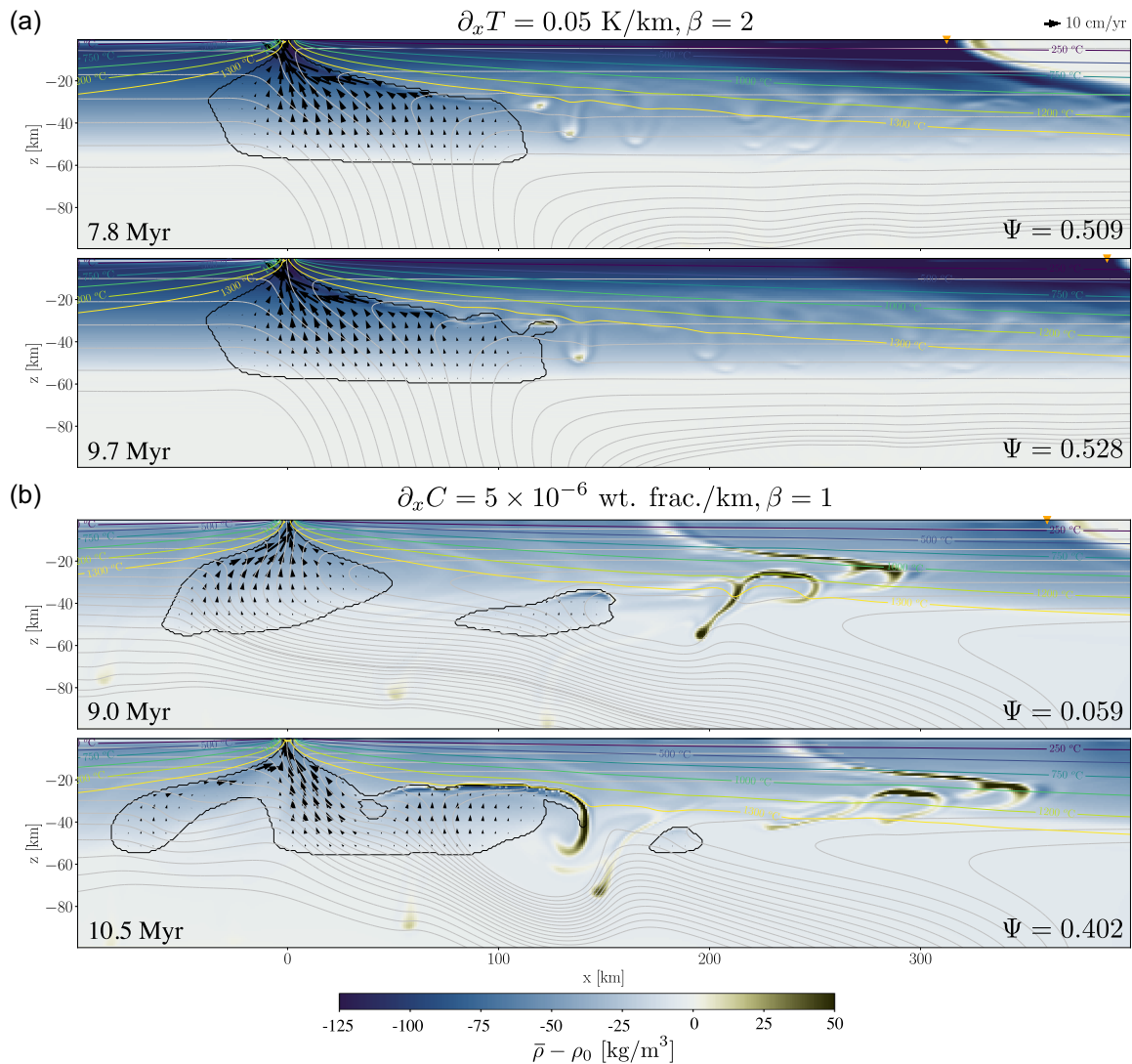


Figure 8. Relative bulk density maps of time-dependent flow in full-ridge models shown at two time steps. (a) Temperature forcing on the bottom boundary $\partial_x T = 0.05 \text{ K km}^{-1}$ and $\beta = 2$ produces small-scale convective instabilities at the solidus. (b) Chemical forcing on the bottom boundary $\partial_x C = 5 \times 10^{-6} \text{ (wt. frac.) km}^{-1}$ and $\beta = 1$ creates large-scale time-dependent flow. Increasing β or the magnitude of forcing increases vigour of convection. Maps show bulk density relative to reference unmolten mantle density (blue represents positively buoyant material, while green represents negatively buoyant material), grey lines represent solid velocity streamlines, black arrows are fluid velocity and black contour is the solidus. See Movies S1, S2 (FR_F1.dTdx005_beta2) and S3, S4 (FR_F2.dCdx5e-6_beta1) for full evolution of each model.

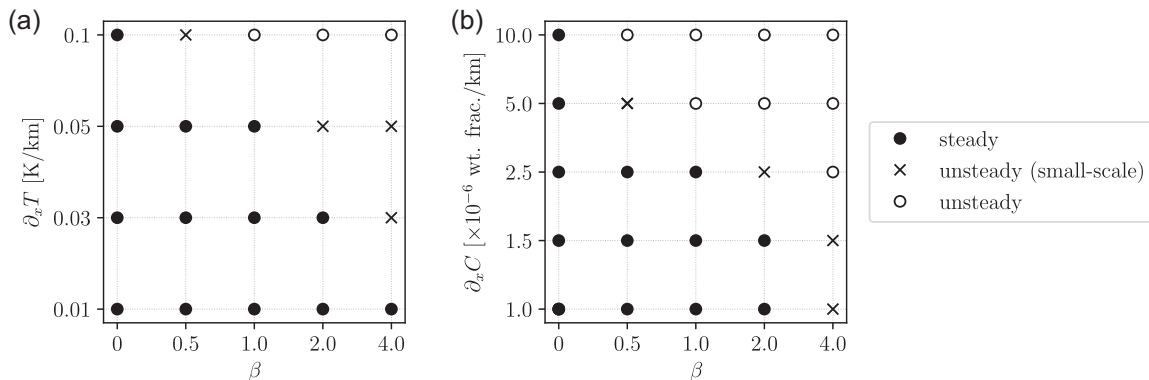


Figure 9. A map of simulation results as a function of the strength of forcing on the y-axis, and β on the x-axis. Each point represents a simulation outcome, in terms of whether the simulation reaches a steady or unsteady state. A transitional regime of small-scale convection at the tip of the partial-melt zone (see Fig. 8a) is marked with crosses. Results obtained with $U_0 = 4 \text{ cm yr}^{-1}$.

variation can lead to pronounced asymmetry for very small forcing ($<1\%$ heterogeneity in the system), which are insufficient in porous-buoyancy-only models. This suggests that long-wavelength mantle heterogeneity (Scheirer *et al.* 1998; Wilson 1992; Harmon *et al.* 2011), perhaps arising from mantle plumes (Phipps Morgan *et al.* 1995; Conder *et al.* 2002; Toomey *et al.* 2002) may induce asymmetry in melt distribution at MORs.

More speculatively, our models support the hypothesis that SSC and melt segregation are important in shaping the LAB (e.g. Rychert *et al.* 2020). We showed that a lateral gradient of composition can trigger time-dependent convective flow beneath the LAB proximal to the ridge, with effects that can reach the ridge axis. In these cases, the melting region varies in shape, topology and position over time. This is in sharp contrast with the roughly triangular melting region associated with corner flow (and with the steady-state results here). A more dynamic arrangement of melting may be consistent with some surface wave tomography results that suggest melt exists over a broad area beneath the ridge out to 400 km off-axis (Forsyth *et al.* 1998). More generally, the interpretation of seismic data (Kawakatsu *et al.* 2009; Rychert *et al.* 2020) is based on an understanding of the plausible distributions of mantle upwelling and melting at MORs. Present results that incorporate density variations introduced by melt segregation alter our understanding of sublithospheric convection and expand the range of plausible behaviours. However, these results are preliminary and require further exploration.

There is evidence that SSC occurs at both young and old lithospheric ages. Melt buoyancy and melt depletion are thought to be important for SSC to occur at young seafloor age [<10 Myr, i.e. Raddick *et al.* (2002); Harmon *et al.* (2020)]. Our time-dependent flow models with $\beta > 0$ support this scenario. Further from the ridge axis, where the thermal boundary layer has thickened substantially, thermal buoyancy will generate convective instabilities at the lithosphere–asthenosphere boundary (e.g. Richter & Parsons 1975; Parsons & McKenzie 1978; Barnouin-Jha *et al.* 1997; Ballmer *et al.* 2009; Likerman *et al.* 2021). The onset time for thermally driven delamination depends on the viscosity contrast between the asthenosphere and the viscous boundary layer at the lithosphere base (Davaille & Jaupart 1994), with earlier onsets associated with lower viscosity contrasts. Investigating the conditions of SSC in both young and old lithosphere, while taking into account melt, compositional and thermal buoyancy, is a goal for future work.

While these results could help interpret a range of observations in terms of buoyancy-driven flow at and near MORs, there are model limitations that affect our findings. First, the model considered here neglects thermal density variations that are certainly important for SSC beneath old oceanic lithosphere and may have subtle effects near the ridge axis. The model can be extended to include thermal buoyancy; scaling analysis in Appendix D derives the relevant thermal buoyancy number. This will be the focus of a future investigation.

The density model also neglects the effect of crystallization/melting sequence at different depths. In our petrological model, we assume a single solid phase with density that depends only on composition. In the natural system, the solid is a poly-phase aggregate, with large density differences between the constituent minerals. The stability and density of mineral phases depends on pressure, temperature and composition; for example, crystallization of basaltic melt yields minerals with different physical bulk properties as a function of depth (Schutt & Leshner 2006; Pearson *et al.* 2021). In the current model, frozen melt is always denser than the

solid residue, which is in contrast to the observation that oceanic crust is less dense than the mantle residue. In future work, the equation of state should be adapted to include the effect of pressure and, perhaps, multiple solid phases should be tracked (Tweed 2021).

We also neglect volatile components that lower the melting temperature, promote deep melting and inhibit shallow crystallization (Hirschmann 2010). This has implications for studying processes at the LAB. Keller *et al.* (2017) explored how volatile-rich reactive channels become subhorizontal melt lenses along the LAB. With ongoing crystallization of these melt lenses, the liquid phase becomes enriched in volatiles, which would have a further influence on density and, potentially, on the interpretation of seismic data (Kawakatsu *et al.* 2009; Schmerr 2012; Rychert *et al.* 2020).

Off-axis melt pooling at the LAB, either intermittent or widespread, may explain intraplate volcanism and petit-spot volcanoes (Hirano *et al.* 2006; Harmon *et al.* 2011). One estimate suggests that to create the total volume of intraplate seamounts would require extraction of $\sim 0.1\%$ molten asthenosphere (Conrad *et al.* 2017). The presence of off-axis volcanism suggests that melt traverses the lithosphere through dikes (Nicolas 1990; Turcotte & Phipps Morgan 1992; Korenaga & Kelemen 1997; Kelemen & Aharonov 1998; Buck *et al.* 2005). Melt that pools at the LAB could thus drain upward in some or all cases (e.g. Havlin *et al.* 2013), an effect not currently included in our models. This would change the location of crystallization and affect the compositional driver of SSC.

The reference compaction length used in this suite of models is ~ 10 km. The compaction length in the asthenosphere may be much shorter, especially if compaction viscosity is controlled by diffusion-creep mechanisms (Rudge 2018a) rather than by viscous deformation of grains (Simpson *et al.* 2010), as assumed here. A shorter compaction length has implications for the efficiency of melt focusing and hence for melt pooling at the LAB, as well as for the prevalence of solitary waves (Sim *et al.* 2020).

5 CONCLUSIONS

We present 2-D, numerical MOR models of the coupled dynamics of liquid magma and the solid mantle. These models build on Katz (2010) to investigate buoyancy-driven mantle flow beneath MORs and, in particular, the consequences of density variation due to Fe/Mg fractionation by melt segregation. The key findings from this study are:

- (i) Compositional density variations create a stable density stratification at depths shallower than the onset of silicate melting beneath MORs. This density stratification partially suppresses the buoyancy-driven upwelling associated with melt retention.
- (ii) However, depletion has important effects on buoyancy-driven flow under long-wavelength mantle heterogeneity. Density variations associated with Fe/Mg fractionation substantially amplify any imposed asymmetry of the mantle source.
- (iii) Such variations may also promote SSC and time-dependent flow and melting beneath MORs, but this requires further exploration. Gravitational instabilities generally develop near the solidus interface, where compositional buoyancy forces due to melting/freezing are important.

Our models of buoyancy-driven flow provide an explanation for the asymmetry of magmatism observed across some MOR axes. Furthermore, these dynamics may be related to observed variations of the lithosphere–asthenosphere boundary.

ACKNOWLEDGMENTS

This research received funding from the European Research Council under Horizon 2020 research and innovation program grant agreement 772255. Numerical simulations were computed on the Arcus-C cluster from the Advanced Research Computing (ARC) services at the University of Oxford. The authors thank T. Davis, D. Rees Jones and S. Toppaladoddi for helpful discussions. Comments by John Naliboff, an anonymous reviewer and editor Juan Carlos Afonso helped to improve the manuscript.

DATA AVAILABILITY

The mid-ocean ridge model is implemented in the code mbuoy3, available at <https://github.com/apusok/FD-PDE.git>. The Github repository also contains the FD-PDE framework described in Appendix C. The version of the code to reproduce the results in this study is available at <https://doi.org/10.5281/zenodo.6900871> (Pusok et al. 2022). The input files and pMELTS Jupyter notebooks to reproduce results in this study are included in the repository. Visualization and post-processing were performed using Python and Scientific Color Maps (Crameri et al. 2020; Crameri 2021). Full simulation data can be requested from AP.

REFERENCES

- Abers, G. A. et al., 2014. Reconciling mantle attenuation-temperature relationships from seismology, petrology, and laboratory measurements, *Geochim. Geophys. Geosyst.*, **15**(9), 3521–3542.
- Afonso, J. & Schutt, D., 2012. The effects of polybaric partial melting on density and seismic velocities of mantle restites, *Lithos*, **134–135**, 289–303.
- Afonso, J., Zlotnik, S. & Fernandez, M., 2008. Effects of compositional and rheological stratifications on small-scale convection under the oceans: implications for the thickness of oceanic lithosphere and seafloor flattening, *Geophys. Res. Lett.*, **35**(20), 1–5.
- Alexiades, V. & Solomon, A.D., 1993. *Mathematical Modeling of Melting and Freezing Processes*, 1st edn, Hemisphere Publishing Corporation.
- Auer, L., Becker, T., Boschi, L. & Schmerr, N., 2015. Thermal structure, radial anisotropy, and dynamics of oceanic boundary layers, *Geophys. Res. Lett.*, **42**, 9740–9749.
- Austin, N. & Evans, R., 2007. A scaling relation for dynamically recrystallized grain size, *Geology*, **35**, 343–346.
- Baker, M. & Stolper, E., 1994. Determining the composition of high-pressure mantle melts using diamond aggregates, *Geochim. Cosmochim. Acta*, **58**(13), 2811–2827.
- Balay, S. et al., 2019. PETSc users manual, Tech. Rep. ANL-95/11 - Revision 3.12, Argonne National Laboratory.
- Ballmer, M., Ito, G., van Hunen, J. & Tackley, P., 2010. Small-scale sublithospheric convection reconciles geochemistry and geochronology of 'superplume' volcanism in the Western and South Pacific, *Earth planet. Sci. Lett.*, **290**(1–2), 224–232.
- Ballmer, M.D., van Hunen, J., Ito, G., Bianco, T.A. & Tackley, P.J., 2009. Intraplate volcanism with complex age–distance patterns: a case for small-scale sublithospheric convection, *Geochim. Geophys. Geosyst.*, **10**(6), 1–22, doi:10.1029/2009GC002386.
- Barnouin-Jha, K., Parmentier, E.M. & Sparks, D.W., 1997. Buoyant mantle upwelling and crustal production at oceanic spreading centers: on-axis segmentation and off-axis melting, *J. geophys. Res.*, **102**(B6), 11 979–11 989.
- Beghein, C., Yuan, K.Q., Schmerr, N. & Xing, Z., 2014. Changes in seismic anisotropy shed light on the nature of the Gutenberg discontinuity, *Science*, **343**(6176), 1237–1240.
- Bell, S., Ruan, Y. & Forsyth, D.W., 2016. Ridge asymmetry and deep aqueous alteration at the trench observed from Rayleigh wave tomography of the Juan De Fuca Plate, *J. geophys. Res.*, **121**, 7298–7321.
- Blackman, D.K. & Kendall, J.M., 1997. Sensitivity of teleseismic body waves to mineral texture and melt in the mantle beneath a mid-ocean ridge, *Phil. Trans. R. Soc. Lond., A*, **355**(1723), 217–231.
- Buck, W., Lavier, L. & Poliakov, A., 2005. Modes of faulting at mid-ocean ridges, *Nature*, **434**, 719–723.
- Buck, W.R. & Parmentier, E.M., 1986. Convection beneath young oceanic lithosphere-implications for thermal structure and gravity, *J. geophys. Res.*, **91**(B2), 1961–1974.
- Buck, W.R. & Su, W.S., 1989. Focused mantle upwelling below mid-ocean ridges due to feedback between viscosity and melting, *Geophys. Res. Lett.*, **16**(7), 641–644.
- Canales, J., Detrick, R., Bazin, S., Harding, A. & Orcutt, J., 1998. Off-axis crustal thickness across and along the East Pacific Rise within the melt area, *Science*, **280**(5367), 1218–1221.
- Choblet, G. & Parmentier, E., 2001. Mantle upwelling and melting beneath slow spreading centers: effects of variable rheology and melt productivity, *Earth planet. Sci. Lett.*, **184**(3), 589–604.
- Clark, A.N. & Leshner, C.E., 2017. Elastic properties of silicate melts: implications for low velocity zones at the lithosphere–asthenosphere boundary, *Sci. Adv.*, **3**(12), 1–5.
- Cline, C.J., Faul, U.H., David, E.C., Berry, A.J. & Jackson, I., 2018. Redox-influenced seismic properties of upper-mantle olivine, *Nature*, **555**(7696), 355–358.
- Cochran, J., 1986. Variations in subsidence rates along intermediate and fast spreading mid-ocean ridges, *Geophys. J. R. astr. Soc.*, **87**(2), 421–454.
- Coltice, N., Husson, L., Faccenna, C. & Arnould, M., 2019. What drives plate tectonics?, *Sci. Adv.*, **5**(10), 1–9.
- Conder, J.A., Forsyth, D.W. & Parmentier, E.M., 2002. Asthenospheric flow and asymmetry of the East Pacific Rise, *J. geophys. Res.*, **107**(B12), 1–10.
- Conrad, C.P., Selway, K., Hirschmann, M.M., Ballmer, M.D. & Wessel, P., 2017. Constraints on volumes and patterns of asthenospheric melt from the space–time distribution of seamounts, *Geophys. Res. Lett.*, **44**, 7203–7210.
- Cormier, M., Macdonald, K. & Wilson, D., 1995. A three-dimensional gravity analysis of the East Pacific Rise from 18° to 21°30'S, *J. geophys. Res.*, **100**(B5), 8063–8082.
- Crameri, F., 2021. Scientific colour maps, Version 7.0.1 (12.09.2021, scm-v7.0).
- Crameri, F., Shephard, G. & Heron, P., 2020. The misuse of colour in science communication, *Nat. Commun.*, **11**(5444), 1–10.
- Davaille, A. & Jaupart, C., 1994. Onset of thermal convection in fluids with temperature-dependent viscosity: application to the oceanic mantle, *J. geophys. Res.*, **99**(B10), 19 853–19 866.
- Davis, E.E. & Karsten, J.L., 1986. On the cause of the asymmetric distribution of seamounts about the Juan De Fuca Ridge: ridge-crest migration over a heterogeneous asthenosphere, *Earth planet. Sci. Lett.*, **79**(3–4), 385–396.
- Evans, R. et al., 1999. Asymmetric electrical structure in the mantle beneath the East Pacific Rise at 17°S, *Science*, **286**(5440), 752–756.
- Faccenda, M., Burlini, L., Gerya, T.V. & Mainprice, D., 2008. Fault-induced seismic anisotropy by hydration in subducting oceanic plates, *Nature*, **455**(7216), 1097–1098.
- Faul, U.H. & Jackson, I., 2005. The seismological signature of temperature and grain size variations in the upper mantle, *Earth planet. Sci. Lett.*, **234**(1–2), 119–134.
- Fleitout, L. & Yuen, D., 1984. Steady state, secondary convection beneath lithospheric plates with temperature- and pressure-dependent viscosity, *J. geophys. Res.*, **89**(B11), 9227–9244.
- Forsyth, D., Harmon, N., Scheirer, D. & Duncan, R., 2006. Distribution of recent volcanism and the morphology of seamounts and ridges in the glimpse study area: implications for the lithospheric cracking hypothesis for the origin of intraplate non-hotspot volcanic chains, *J. geophys. Res.*, **111**(11), 1–19.
- Forsyth, D., Webb, S., Dorman, L. & Shen, Y., 1998. Phase velocities of Rayleigh waves in the melt experiment on the East Pacific Rise, *Science*, **280**(5367), 1235–1238.

- Forsyth, D.W. & Chave, A., 1994. Experiment investigates magma in the mantle beneath mid-ocean ridges, *EOS, Trans. Am. geophys. Un.*, **75**, 537–540.
- Gaherty, J.B., Kato, M. & Jordan, T.H., 1999. Seismological structure of the upper mantle: a regional comparison of seismic layering, *Phys. Earth planet. Inter.*, **110**(1–2), 21–41.
- Ghiorso, M. & Wolf, A., 2019. Thermodynamic modeling using ENKI: 1. Overview and phase equilibrium applications, in *AGU Fall Meeting Abstracts*, abstract #ED53F-0897, AGU.
- Ghiorso, M.S., Hirschmann, M.M., Reiners, P.W. & Kress, V.C., 2002. The pMELTS: a revision of MELTS for improved calculation of phase relations and major element partitioning related to partial melting of the mantle to 3 GPa, *Geochem. Geophys. Geosyst.*, **3**(5), 1–36.
- Ghods, A. & Arkani-Hamed, J., 2000. Melt migration beneath mid-ocean ridges, *Geophys. J. Int.*, **140**, 687–697.
- Gripp, A. & Gordon, R., 1990. Current plate velocities relative to the hotspots incorporating the NUVEL-1 global plate motion model, *Geophys. Res. Lett.*, **17**(8), 1109–1112.
- Hansen, L., Faccenda, M. & Warren, J., 2021. A review of mechanisms generating seismic anisotropy in the upper mantle, *Phys. Earth planet. Inter.*, **313**, 106662.
- Harmon, N., Forsyth, D., Weeraratne, D., Yang, Y. & Webb, S., 2011. Mantle heterogeneity and off axis volcanism on young Pacific lithosphere, *Earth Planet. Sci. Lett.*, **311**(3–4), 306–315.
- Harmon, N., Rychert, C., Kendall, J., Tharimena, S., Bogiatzis, P. & Agius, M., 2020. Evolution of the oceanic lithosphere in the equatorial Atlantic from Rayleigh wave tomography, evidence for small-scale convection from the PI-LAB experiment, *Geochem. Geophys. Geosyst.*, **21**(9), 1–18.
- Havlin, C., Parmentier, E. & Hirth, G., 2013. Dike propagation driven by melt accumulation at the lithosphere–asthenosphere boundary, *Earth planet. Sci. Lett.*, **376**, 20–28.
- Haxby, W.F. & Weissel, J.K., 1986. Evidence for small-scale mantle convection from Seasat altimeter data, *J. geophys. Res.*, **91**(B3), 3507–3520.
- Herlund, J., Tackley, P. & Stevenson, D., 2008. Buoyant melting instabilities beneath extending lithosphere: 1. Numerical models, *J. geophys. Res.*, **113**(B4), 1–17.
- Hewitt, I.J. & Fowler, A.C., 2008. Partial melting in an upwelling mantle column, *Proc. R. Soc., A*, **464**(2097), 2467–2491.
- Hirano, N. *et al.*, 2006. Volcanism in response to plate flexure, *Science*, **313**(5792), 1426–1428.
- Hirschmann, M., 2010. Partial melt in the oceanic low velocity zone, *Phys. Earth planet. Inter.*, **179**, 60–71.
- Hirth, G. & Kohlstedt, D., 2003. Rheology of the upper mantle and the mantle wedge: a view from the experimentalists, in *Inside the Subduction Factory*, Vol. **138**, pp. 83–105, ed. Eiler, J., Geophysical Monograph American Geophysical Union.
- Hofmann, A., 1997. Mantle geochemistry: the message from oceanic volcanism, *Nature*, **385**, 219–229.
- Ito, G. & Dunn, R.A., 2009. Mid-ocean ridges: mantle convection and formation of the lithosphere, in *Encyclopedia of Ocean Sciences*, pp. 867–880, eds Steele, J.H., Turekian, K.K. & Thorpe, S.A., Academic Press.
- Jha, K., Parmentier, E.M. & Phipps Morgan, J., 1994. The role of mantle depletion and melt-retention buoyancy in spreading-center segmentation, *Earth planet. Sci. Lett.*, **125**(1–4), 221–234.
- Johansen, S., Panzner, M., Mittet, R., Amundsen, H., Lim, A., Vik, E., Landrø, M. & Arntsen, B., 2019. Deep electrical imaging of the ultraslow-spreading Mohs Ridge, *Nature*, **567**, 379–383.
- Karato, S.-I., 2003. Mapping water content in upper mantle. in *Inside the subduction factory*, *Geophys. Monogr. Ser., AGU*, **138**, 135–152.
- Karato, S.-I., 2012. On the origin of the asthenosphere, *Earth planet. Sci. Lett.*, **321**–**322**, 95–103.
- Karato, S. & Wu, P., 1993. Rheology of the upper mantle—a synthesis, *Science*, **260**(5109), 771–778.
- Karato, S.I., Olugboji, T. & Park, J., 2015. Mechanisms and geologic significance of the mid-lithosphere discontinuity in the continents, *Nat. Geosci.*, **8**(7), 509–514.
- Katz, R., 2008. Magma dynamics with the enthalpy method: benchmark solutions and magmatic focusing at mid-ocean ridges, *J. Petrol.*, **49**(12), 2099–2121.
- Katz, R., 2010. Porosity-driven convection and asymmetry beneath mid-ocean ridge, *Geochem. Geophys. Geosyst.*, **11**, 1–29.
- Katz, R. & Weatherley, S., 2012. Consequences of mantle heterogeneity for melt extraction at mid-ocean ridges, *Earth planet. Sci. Lett.*, **335**–**336**, 226–237.
- Katz, R.F., 2022. *The Dynamics of Partially Molten Rock*, 1st edn, Princeton Univ. Press.
- Katz, R.F., Jones, D.W.R., Rudge, J.F. & Keller, T., 2022. Physics of melt extraction from the mantle: speed and style, *Ann. Rev. Earth planet. Sci.*, **50**, 507–540.
- Katz, R.F., Knepley, M.G., Smith, B., Spiegelman, M. & Coon, E.T., 2007. Numerical simulation of geodynamic processes with the portable extensible toolkit for scientific computation, *Phys. Earth planet. Inter.*, **163**, 52–68.
- Kawakatsu, H., Kumar, P., Takei, Y., Shinohara, M., Kanazawa, T., Araki, E. & Suyehiro, K., 2009. Seismic evidence for sharp lithosphere–asthenosphere boundaries of oceanic plates, *Science*, **324**(5926), 499–502.
- Kelemen, P. & Aharonov, E., 1998. Periodic formation of magma fractures and generation of layered gabbros in the lower crust beneath oceanic spreading ridges, in *Faulting and Magmatism at Mid-Ocean Ridges*, *Geophysical Monograph Series*, Vol. **106**, pp. 267–289, eds Buck, W.R., Delaney, P.T., Karson, J.A. & Lagabriele, Y., AGU.
- Keller, T., Katz, R.F. & Hirschmann, M.M., 2017. Volatiles beneath mid-ocean ridges: deep melting, channelised transport, focusing, and metasomatism, *Earth planet. Sci. Lett.*, **464**, 55–68.
- Keller, T., May, D. & Kaus, B., 2013. Numerical modelling of magma dynamics coupled to tectonic deformation of lithosphere and crust, *Geophys. J. Int.*, **195**(3), 1406–1442.
- Key, K., Constable, S., Liu, L. & Pommier, A., 2013. Electrical image of passive mantle upwelling beneath the northern East Pacific Rise, *Nature*, **495**, 499–502.
- Korenaga, J. & Kelemen, P., 1997. Origin of gabbro sills in the Moho transition zone of the oman ophiolite: implications for magma transport in the oceanic lower crust, *J. geophys. Res.*, **102**, 729–749.
- Langmuir, C.H., Klein, E. & Plank, T., 1992. Petrological systematics of mid-oceanic ridge basalts: constraints on melt generation beneath ocean ridges, in *Mantle Flow and Melt Generation at Mid-Ocean Ridges*, Vol. **71**, pp. 183–280, eds Morgan, J.P., Blackman, D.K. & Sinton, J.M., AGU.
- Likerman, J., Zlotnik, S. & Li, C.-F., 2021. The effects of small-scale convection in the shallow lithosphere of the North Atlantic, *Geophys. J. Int.*, **227**(3), 1512–1522.
- Mammerickx, J. & Taylor, I.L., 1971. Bathymetry of the pioneer survey area, north of 45°N latitude, Scripps Inst. Oceanogr., Geol. Data Center, Spec. Chart No. 1.
- Marjanovic, M., Carbotte, S.M., Nedimovic, M.R. & Canales, J.P., 2011. Gravity and seismic study of crustal structure along the Juan De Fuca ridge axis and across pseudofaults on the ridge flanks, *Geochem. Geophys. Geosyst.*, **12**(Q05008), 1–22.
- McKenzie, D., 1969. Speculations on the consequences and causes of plate motion, *Geophys. J. R. astr. Soc.*, **18**(1), 1–32.
- McKenzie, D., 1984. The generation and compaction of partially molten rock, *J. Petrol.*, **25**(3), 713–765.
- McKenzie, D. & Bickle, M.J., 1988. The volume and composition of melt generated by extension of the lithosphere, *J. Petrol.*, **29**(3), 625–679.
- McManus, D., 1967. Physiography of Cobb and Gorda rises, northeast Pacific Ocean, *Geol. Soc. Am. Bull.*, **78**(4), 527–546.
- Mehouachi, F. & Singh, S., 2018. Water-rich sublithospheric melt channel in the equatorial Atlantic Ocean, *Nat. Geosci.*, **11**, 65–69.
- Naif, S., Key, K., Constable, S. & Evans, R.L., 2013. Melt-rich channel observed at the lithosphere–asthenosphere boundary, *Nature*, **495**(7441), 356–359.
- Nicolas, A., 1990. Melt extraction from mantle peridotites: hydrofracturing or porous flow consequences on oceanic ridge activity, in *Magma Transport and Storage*, pp. 160–174, ed. Ryan, M.P., Wiley.

- Olive, J.-A. & Dublanchet, P., 2020. Controls on the magmatic fraction of extension at mid-ocean ridges, *Earth planet. Sci. Lett.*, **549**(116541), 1–10.
- Oxburgh, E.R. & Parmentier, E.M., 1977. Compositional and density stratification in oceanic lithosphere: causes and consequences, *J. Geol. Soc. Lond.*, **133**(4), 343–355.
- Parmentier, E. & Phipps Morgan, J., 1990. Spreading rate dependence of 3-dimensional structure in oceanic spreading centers, *Nature*, **348**, 325–328.
- Parsons, B. & McKenzie, D., 1978. Mantle convection and the thermal structure of the plates, *J. geophys. Res.*, **83**(B9), 4485–4496.
- Parsons, B. & Sclater, J.G., 1977. An analysis of the variation of ocean floor bathymetry and heat flow with age, *J. geophys. Res.*, **82**(5), 803–827.
- Pearson, D. *et al.*, 2021. Deep continental roots and cratons, *Nature*, **596**, 199–210.
- Phipps Morgan, J., Morgan, W., Zhang, Y.-S. & Smith, W., 1995. Observational hints for a plume fed, suboceanic asthenosphere and its role in mantle convection, *J. geophys. Res.*, **100**(12), 12 753–12 767.
- Phipps Morgan, J., Parmentier, E. & Lin, J., 1987. Mechanisms for the origin of mid-ocean ridge axial topography: implications for the thermal and mechanical structure of accreting plate boundaries, *J. geophys. Res.*, **92**(B12), 12 823–12 836.
- Pilet, S. *et al.*, 2016. Pre-subduction metasomatic enrichment of the oceanic lithosphere induced by plate exure, *Nat. Geosci.*, **9**(12), 898–903.
- Pusok, A., May, D., Li, Y. & Katz, R., 2022. FD-PDE framework: v1.0.0.
- Qin, Y., Singh, S., Grevemeyer, I., Marjanovic, M. & Buck, W., 2020. Discovery of flat seismic reflections in the mantle beneath the young Juan de Fuca plate, *Nat. Commun.*, **11**(4122), 1–12.
- Rabinowicz, M., Nicolas, A. & Vigneresse, J.L., 1984. A rolling-mill effect in the asthenosphere beneath oceanic spreading centers, *Earth planet. Sci. Lett.*, **67**, 97–108.
- Raddick, M.J., Parmentier, E.M. & Scheirer, D.S., 2002. Buoyant decompression melting: a possible mechanism for intraplate volcanism, *J. geophys. Res.*, **107**(B10), 1–11.
- Rader, E., Emry, E., Schmerr, N., Frost, D., Cheng, C., Menard, J., Yu, C.-Q. & Geist, D., 2015. Characterization and petrological constraints of the mid-lithospheric discontinuity, *Geochem., Geophys., Geosyst.*, **16**, 3484–3504.
- Ribe, N.M., 1985. The generation and composition of partial melts in the Earth's mantle, *Earth planet. Sci. Lett.*, **73**(2), 361–376.
- Richter, F., 1973. Convection and the large-scale circulation of the mantle, *J. geophys. Res.*, **78**(35), 8735–8745.
- Richter, F. & Parsons, B., 1975. On the interaction of two scales of convection in the mantle, *J. geophys. Res.*, **80**(17), 2529–2541.
- Ritzwoller, M.H., Shapiro, N.M. & Zhong, S.J., 2004. Cooling history of the Pacific lithosphere, *Earth planet. Sci. Lett.*, **226**(1–2), 69–84.
- Roache, P.J., 2002. Code verification by the method of manufactured solutions, *J. Fluids Eng.*, **124**(1), 4–10.
- Rubin, K.H. & Sinton, J.M., 2007. Inferences on mid-ocean ridge thermal and magmatic structure from MORB compositions, *Earth planet. Sci. Lett.*, **260**(1–2), 257–276.
- Rudge, J., 2018a. The viscosities of partially molten materials undergoing diffusion creep, *J. geophys. Res.*, **123**(12), 10 534–10 562.
- Rudge, J., *et al.* 2018b. Textural equilibrium melt geometries around tetrakaidecahedral grains, *Proc. R. Soc. A.*, **474**(2212), 1–24, doi:10.1098/rspa.2017.0639.
- Rychert, C., Harmon, N., Constable, S. & Wang, S., 2020. The nature of the lithosphere-asthenosphere boundary, *J. geophys. Res.*, **125**(10), e2018JB016463, doi:10.1029/2018JB016463.
- Rychert, C.A. *et al.*, 2021. A dynamic lithosphere-asthenosphere boundary near the equatorial mid-Atlantic ridge, *Earth planet. Sci. Lett.*, **566**, 1–11.
- Rychert, C.A. & Shearer, P.M., 2009. A global view of the lithosphere-asthenosphere boundary, *Science*, **324**(5926), 495–498.
- Sanan, P., May, D., Mills, R. & Kaus, B., 2022. DMStag: staggered, structured grids for PETSc, *J. Open Sour. Softw.*, in review, 1–5.
- Scheirer, D., Forsyth, D., Cormier, M. & MacDonald, K., 1998. Shipboard geophysical indications of asymmetry and melt production beneath the East Pacific Rise near the melt experiment, *Science*, **280**(5367), 1221–1224.
- Schmerr, N., 2012. The Gutenberg discontinuity: melt at the lithosphere-asthenosphere boundary, *Science*, **335**(6075), 1480–1483.
- Schutt, D.L. & Leshner, C.E., 2006. Effects of melt depletion on the density and seismic velocity of garnet and spinel lherzolite, *J. geophys. Res.*, **111**(B5), 1–24.
- Scott, D.R. & Stevenson, D.J., 1989. A self-consistent model of melting, magma migration and buoyancy-driven circulation beneath mid-ocean ridges, *J. geophys. Res.*, **94**(B3), 2973–2988.
- Selway, K., Ford, H. & Kelemen, P., 2015. The seismic mid-lithosphere discontinuity, *Earth planet. Sci. Lett.*, **414**, 45–57.
- Selway, K. & O'Donnell, J.P., 2019. A small, unextractable melt fraction as the cause for the low velocity zone, *Earth planet. Sci. Lett.*, **517**, 117–124.
- Sim, S.J., Spiegelman, M., Stegman, D.R. & Wilson, C., 2020. The influence of spreading rate and permeability on melt focusing beneath mid-ocean ridges, *Phys. Earth planet. Inter.*, **304**(106486), 1–17.
- Simpson, G., Spiegelman, M. & Weinstein, M., 2010. A multiscale model of partial melts: 1. Effective equations, *J. geophys. Res.*, **115**(B04410), 1–17.
- Small, C. & Danyushevsky, L.V., 2003. Plate-kinematic explanation for mid-oceanic-ridge depth discontinuities, *Geology*, **31**(5), 399–402.
- Sotin, C. & Parmentier, E.M., 1989. Dynamical consequences of compositional and thermal density stratification beneath spreading centers, *Geophys. Res. Lett.*, **16**(8), 835–838.
- Sparks, D.W. & Parmentier, E.M., 1993. The structure of 3-dimensional convection beneath oceanic spreading centers, *Geophys. J. Int.*, **112**(1), 81–91.
- Spiegelman, M., 1993. Physics of melt extraction: theory, implications and applications, *Phil. Trans. R. Soc. Lond. A*, **342**, 23–41.
- Spiegelman, M. & Reynolds, J.R., 1999. Combined dynamic and geochemical evidence for convergent melt flow beneath the East Pacific Rise, *Nature*, **402**, 282–285.
- Stein, C. & Stein, S., 1992. A model for the global variation in oceanic depth and heat flow with lithospheric age, *Nature*, **359**(6391), 123–129.
- The Melt Seismic Team, 1998. Imaging the deep seismic structure beneath a mid-ocean ridge: the MELT experiment, *Science*, **280**(5367), 1215–1218.
- Tolstoy, M., Harding, A.J. & Orcutt, J., 1993. Crustal thickness on the mid-Atlantic ridge: bull's-eye gravity anomalies and focused accretion, *Science*, **262**(5134), 726–729.
- Toomey, D., Wilcock, W., Conder, J.A., Forsyth, D.W., Blundy, J.D., Parmentier, E.M. & Hammond, W.C., 2002. Asymmetric mantle dynamics in the melt region of the East Pacific Rise, *EPSL*, **200**(3–4), 287–295.
- Toomey, D., Wilcock, W., Solomon, S., Hammond, W. & Orcutt, J., 1998. Mantle seismic structure beneath the melt region of the East Pacific Rise from P and S wave tomography, *Science*, **280**(5367), 1224–1227.
- Toomey, D.R. *et al.*, 2014. The Cascadia initiative: a sea change in seismological studies of subduction zones, *Oceanography*, **27**, 138–150.
- Turcotte, D. & Phipps Morgan, J., 1992. The physics of magma migration and mantle flow beneath a mid-ocean ridge, in *Mantle Flow and Melt Generation at Mid-Ocean Ridges*, Geophys. Monogr. Ser., Vol. 71, pp. 155–182, eds Morgan, J. P., Blackman, D. K. & Sinton, J. M., AGU.
- Turcotte, D. & Schubert, G., 2014. *Geodynamics*, 3rd edn, Cambridge Univ. Press.
- Turner, J.S., 1973. *Buoyancy Effects in Fluids*, 1st edn, Cambridge Univ. Press.
- Tweed, L.E.L., 2021. Coupling the thermodynamics, kinetics and geodynamics of multiphase reactive transport in Earth's interior, *PhD thesis*, Columbia University, New York, NY.
- van Hunen, J. & Zhong, S., 2006. Influence of rheology on realignment of mantle convective structure with plate motion after a plate reorganization, *Geochem. Geophys. Geosyst.*, **7**(8), doi:10.1029/2005GC001209.
- Vlastélic, I., Aslanian, D., Dosso, L., Bougault, H., Olivet, J. & Géli, L., 1999. Large-scale chemical and thermal division of the Pacific mantle, *Nature*, **399**, 345–350.
- Walter, M., 1998. Melting of garnet peridotite and the origin of komatiite and depleted lithosphere, *J. Petrol.*, **39**(1), 29–60.

- Wang, S., Constable, S., Rychert, C. & Harmon, N., 2020. A lithosphere–asthenosphere boundary and partial melt estimated using marine magnetotelluric data at the central middle Atlantic Ridge, *Geochem. Geophys. Geosyst.*, **21**(9), 1–17.
- Wang, Y., Forsyth, D.W. & Savage, B., 2009. Convective upwelling in the mantle beneath the Gulf of California, *Nature*, **462**(7272), 499–501.
- Wark, D., 2003. Reassessment of pore shapes in microstructurally equilibrated rocks, with implications for permeability of the upper mantle, *J. geophys. Res.*, **108**(B1), doi:10.1029/2001JB001575.
- Wark, D. & Watson, E., 1998. Grain-scale permeabilities of texturally equilibrated, monomineralic rocks, *Earth. planet. Sci. Lett.*, **164**(3–4), 591–605.
- White, R.S., Minshull, T.A., Bickle, M.J. & Robinson, C.J., 2001. Melt generation at very slow-spreading oceanic ridges: constraints from geochemical and geophysical data, *J. Petrol.*, **42**(6), 1171–1196.
- Wilson, D., 1992. Focused mantle upwelling beneath mid-ocean ridges: evidence from seamount formation and isostatic compensation of topography, *Earth. planet. Sci. Lett.*, **113**(1), 41–55.
- Wolfe, C. & Solomon, S., 1998. Shear-wave splitting and implications for mantle flow beneath the melt region of the East Pacific Rise, *Science*, **280**(5367), 1230–1232.
- Yamauchi, H. & Takei, Y., 2016. Polycrystal anelasticity at near-solidus temperatures, *J. geophys. Res.*, **121**, 7790–7820.
- Yang, J. & Faccenda, M., 2020. Intraplate volcanism originating from upwelling hydrous mantle transition zone, *Nature*, **579**, 88–91.
- Yang, Y., Forsyth, D.W. & Weeraratne, D.S., 2007. Seismic attenuation near the East Pacific Rise and the origin of the low-velocity zone, *Earth. planet. Sci. Lett.*, **258**(1–2), 260–268.
- Zlotnik, S., Afonso, J., Diez, P. & Fernandez, M., 2008. Small-scale gravitational instabilities under the oceans: implications for the evolution of oceanic lithosphere and its expression in geophysical observables, *Philos. Mag.*, **88**(28–29), 3197–3217.

SUPPORTING INFORMATION

Supplementary data are available at [GJI](https://doi.org/10.1017/jfm.2023.1556) online.

Movie S1. FR_F1_dTdx005_beta2-porosity.mp4 - Porosity field in full-ridge model with thermal forcing.

Movie S2. FR_F1_dTdx005_beta2-rho-zoom.mp4 - Relative density field in full-ridge model with thermal forcing.

Movie S3. FR_F2_dCdx5e-6_beta1-porosity.mp4 - Porosity field in full-ridge model with chemical forcing.

Movie S4. FR_F2_dCdx5e-6_beta1-rho-zoom.mp4 - Relative density field in full-ridge model with chemical forcing.

Please note: Oxford University Press is not responsible for the content or functionality of any supporting materials supplied by the authors. Any queries (other than missing material) should be directed to the corresponding author for the paper.

APPENDIX A: GOVERNING EQUATIONS

The model below is an extension to the theory described in Katz (2008, 2010). The theory is based on the McKenzie (1984) equations and consists of a set of coupled partial differential equations representing conservation of mass, momentum, energy and composition in a two-phase, two-component medium. The two phases comprise a high-viscosity deformable and permeable solid (subscript s), which makes up the vast bulk of the mantle, and a low-viscosity liquid phase (subscript ℓ), representing the magma. The derivation is motivated by the understanding that magma is produced by partial melting of mantle rocks and is distributed in a connected network of narrow pores between solid grains. This theory is combined with the Enthalpy Method for modelling the thermodynamics of melting of a multicomponent system (Alexiades & Solomon 1993; Katz

2008). Values for reference parameters are given in Table 1. For a didactic introduction to the theory see Katz (2022).

A1 Phase densities, pressure decomposition and reformulation of mechanics

We use linearized equations of state for phase densities

$$\rho_i = \rho_{0i}(1 - B_i), \quad (\text{A1})$$

with $B_i = \alpha(T - T_0) + \beta(C_i - C_0)$, where α and β are coefficients of thermal and compositional expansion and i represents phase (liquid, solid). The constants ρ_{s0} , $\rho_{\ell0}$, T_0 , C_0 are reference values. Appendix E provides pMELTS estimates for β . The thermal expansivity α , taken zero in the buoyancy term in the main text, is included in the derivation below.

We decompose the liquid pressure as in Katz (2010)

$$P_\ell = P_{\text{lith}} + P + \mathcal{P}, \quad (\text{A2})$$

where $P_{\text{lith}} = -\rho_{s0}gz$ is the lithostatic pressure, P is dynamic pressure, and $\mathcal{P} = (\zeta - 2\eta/3)\nabla \cdot \mathbf{v}_s$ is the compaction pressure. Eqs (5) and (6) become

$$-\nabla P + \nabla \cdot \eta(\nabla \mathbf{v}_s + \nabla \mathbf{v}_s^T) - (\phi \Delta \rho + \overline{\rho_0 B})\mathbf{g} = \mathbf{0}, \quad (\text{A3})$$

$$\nabla \cdot \mathbf{v}_s - \nabla \cdot \frac{K}{\mu} [\nabla P + \nabla \mathcal{P} + (\Delta \rho + \rho_{\ell0} B_\ell)\mathbf{g}] = 0, \quad (\text{A4})$$

where $\Delta \rho = \rho_{s0} - \rho_{\ell0}$, and $\overline{\rho_0 B} = \phi \rho_{\ell0} B_\ell + (1 - \phi) \rho_{s0} B_s$. The term $(\phi \Delta \rho + \rho_{\ell0} B_\ell)\mathbf{g}$ is the buoyancy term in momentum eq. (A3) that is explored further in scaling analysis in Appendix D.

A2 Energy and composition, enthalpy method

Conservation laws for energy and composition are given in eqs (7) and (8). The relationship between temperature T and potential temperature \mathcal{T} is

$$T = \mathcal{T} \exp(-\alpha gz/c_p), \quad (\text{A5})$$

where z is vertical coordinate beneath surface (i.e. $z \in [-H, 0]$, negative of depth).

Eqs (7) and (8) are solved in terms of enthalpy \mathcal{H} and bulk composition C , so four closure equations are required to determine \mathcal{T} , ϕ , C_s , C_ℓ . The enthalpy method (Alexiades & Solomon 1993) provides these if we assume thermal equilibrium in a two-phase, two-component system and neglect variations in partial specific entropy,

$$\mathcal{H} = \rho \mathcal{L} \phi + \rho c_p (T - T_0), \quad (\text{A6})$$

$$C = \phi C_\ell + (1 - \phi) C_s, \quad (\text{A7})$$

$$C_s = f_s(T, P_{\text{lith}}), \quad (\text{A8})$$

$$C_\ell = f_\ell(T, P_{\text{lith}}). \quad (\text{A9})$$

The first equation is the definition of bulk enthalpy, and says that the enthalpy equals the sum of the latent and sensible energy. The second equation is the definition of bulk composition, while the third and fourth are the solidus and liquidus equations. The liquidus and solidus specify the composition of the coexisting solid and liquid phases in equilibrium at a given pressure and temperature (see Section A3.1). These can be combined to give an equation for porosity

$$\phi f_\ell(T, P_{\text{lith}}) + (1 - \phi) f_s(T, P_{\text{lith}}) - C = 0. \quad (\text{A10})$$

A3 Constitutive equations

The constitutive equations for phase densities, bulk density, shear and compaction viscosity and permeability are given in the main text in eqs (1), (2), (9), (10) and (11).

In addition, we define $T_{\eta_0} = T_p \exp(\alpha g z_m / c_p)$, where $z_m > 0$ is the melting depth. The depth of melting is controlled primarily by the potential mantle temperature and is calculated as

$$z_m = \frac{\gamma c_p (T_p - T_0)}{g(\rho_0 c_p - \gamma T_p \alpha)}. \quad (\text{A11})$$

The shear viscosity is confined to a limited range according to

$$\eta' = \left(\frac{1}{\eta} + \frac{1}{\eta_{\max}} \right)^{-1} + \eta_{\min}, \quad (\text{A12})$$

where η is viscosity calculated in eq. (9), and values for η_{\min} and η_{\max} are given in Table 1.

To avoid $\zeta \rightarrow \infty$ when $\phi \rightarrow 0$, we regularize the compaction viscosity (Simpson *et al.* 2010) as

$$\zeta' = \zeta_0 \exp \left[\frac{E_A}{R} \left(\frac{1}{T} - \frac{1}{T_{\eta_0}} \right) \right] \frac{1}{\phi + \phi_{\min}}. \quad (\text{A13})$$

A3.1 Petrology and phase diagram

Petrological relations are parameterized with a two-phase, two-component phase diagram (Katz & Weatherley 2012). This defines an equilibrium between temperature, lithostatic pressure and phase compositions for the two-component system. The solidus and liquidus temperatures increase linearly with pressure according to the Clapeyron slope; the compositional dependence is linearized from a binary phase loop (Katz 2022). The surfaces are defined by

$$C_s = C_0 + \frac{T - (T_0 + P_{\text{lith}}/\gamma)}{M}, \quad (\text{A14})$$

$$C_\ell = C_0 - \Delta C + \frac{T - (T_0 + P_{\text{lith}}/\gamma)}{M}, \quad (\text{A15})$$

where C_ℓ , C_s are the compositions of the solid and liquid, respectively, where they coexist in thermodynamic equilibrium. T_0 is the reference solidus temperature at zero pressure and ambient mantle composition C_0 , ΔC is the composition difference between solidus and liquidus surfaces, P_{lith} is the lithostatic pressure, $\gamma = \partial P_{\text{lith}} / \partial T|_{C_i}$ is the Clapeyron slope (equal between phases). The change in temperature with composition at fixed pressure, also assumed equal between phases, is given by $M = \partial T / \partial C_i|_{P_{\text{lith}}}$.

APPENDIX B: NON-DIMENSIONALIZATION

To non-dimensionalize the above equations, we use the following variables

$$\theta = \frac{T - T_0}{\Delta T}, \quad \tilde{\theta} = \frac{T - T_0}{\Delta T}, \quad \Theta_i = \frac{C_i - C_0}{\Delta C}, \quad (\text{B1})$$

where $\Delta T = M \Delta C$. We also define the following characteristic scales

$$[x] = H, \quad [\mathbf{v}] = w_0, \quad w_0 = \frac{K_0 \Delta \rho g}{\mu}, \quad (\text{B2})$$

$$[t] = \frac{H}{w_0}, \quad [K] = K_0, \quad [P] = H \Delta \rho g, \quad (\text{B3})$$

$$[\eta, \zeta, \xi] = \eta_0, \quad [\rho]^{PV} = \Delta \rho, \quad [\rho]^{HC} = \rho_0, \quad (\text{B4})$$

$$[\mathcal{H}] = \rho_0 c_p \Delta T, \quad [\Gamma, S] = \frac{w_0 \rho_0}{H} \quad (\text{B5})$$

where H is characteristic domain size (i.e. domain height), w_0 is the characteristic Darcy velocity, K_0 is the permeability prefactor, η_0 is reference viscosity, $\Delta \rho = \rho_{s0} - \rho_{\ell 0}$ and ρ_0 is a reference density. The density in the mechanics system of equations (PV) is scaled with $\Delta \rho$, while the density in the energy and composition equations (HC) is scaled with ρ_0 .

The non-dimensional system of equations for the mechanics becomes

$$-\nabla P + \delta^2 \nabla \cdot \eta (\nabla \mathbf{v}_s + \nabla \mathbf{v}_s^T) - (\phi + \mathcal{B}) \hat{\mathbf{k}} = \mathbf{0}, \quad (\text{B6})$$

$$\nabla \cdot \mathbf{v}_s - \nabla \cdot K [\nabla P + \nabla \mathcal{P} + (1 + \mathcal{B}_\ell) \hat{\mathbf{k}}] = 0, \quad (\text{B7})$$

$$\nabla \cdot \mathbf{v}_s - \frac{\mathcal{P}}{\delta^2 \xi} = 0, \quad (\text{B8})$$

where $\xi = \zeta - \frac{2}{3}\eta$ and δ is a non-dimensional compaction length defined as

$$\delta = \frac{1}{H} \left(\frac{K_0 \eta_0}{\mu} \right)^{1/2}. \quad (\text{B9})$$

The non-dimensional buoyancy terms can be written as

$$\mathcal{B} = \frac{\rho_0 \bar{B}}{\Delta \rho} = \frac{\rho_0}{\Delta \rho} \alpha^* \tilde{\theta} + \frac{\rho_0}{\Delta \rho} \beta^* \Theta - \phi \alpha^* \tilde{\theta} - \phi \beta^* \Theta_\ell, \quad (\text{B10})$$

$$\mathcal{B}_\ell = \frac{\rho_{\ell 0} B_\ell}{\Delta \rho} = \frac{\rho_0}{\Delta \rho} \alpha^* \tilde{\theta} + \frac{\rho_0}{\Delta \rho} \beta^* \Theta_\ell - \alpha^* \tilde{\theta} - \beta^* \Theta_\ell, \quad (\text{B11})$$

where the solid density is taken as the reference density $\rho_{s0} = \rho_0$, $\rho_{\ell 0} = \rho_0 - \Delta \rho$ and $\Theta = \phi \Theta_\ell + (1 - \phi) \Theta_s$. Parameters α^* and β^* are defined in Table B1. In the above equations, we will ignore density variations in the fluid phase ($\mathcal{B}_\ell = 0$), as we are only interested in the effect of buoyancy due to melting on the solid phase in the momentum balance. Non-zero \mathcal{B}_ℓ will lead to porous convection in the fluid phase, which can cause problems for time-stepping.

To non-dimensionalize the energy and composition eqs (7) and (8), we assume constant density $\rho = \rho_0$ to obtain

$$\frac{\partial \mathcal{H}}{\partial t} + e^{-\mathcal{A}z} \nabla \cdot \tilde{\mathbf{v}} \theta = S \nabla \cdot (1 - \phi) \mathbf{v}_s + \frac{1}{Pe_T} e^{-\mathcal{A}z} \nabla^2 \theta \quad (\text{B12})$$

$$\frac{\partial \Theta}{\partial t} + \nabla \cdot \phi \mathbf{v}_\ell \Theta_\ell + \nabla \cdot (1 - \phi) \mathbf{v}_s \Theta_s = \frac{1}{Pe_C} \nabla \cdot \phi \nabla \Theta_\ell, \quad (\text{B13})$$

where \mathcal{A} is the adiabatic parameter, z is non-dimensional vertical coordinate, S is the Stefan number, Pe_T is the thermal Peclet number, κ is thermal diffusivity and Pe_C is the compositional Peclet number (Table B1).

The non-dimensional form for porosity and closure eqs (A6)–(A10) in the enthalpy method are

$$\mathcal{H} = S \phi + \tilde{\theta}, \quad (\text{B14})$$

$$\Theta_s = \tilde{\theta} - G P_{\text{lith}}, \quad (\text{B15})$$

$$\Theta_\ell = \tilde{\theta} - G P_{\text{lith}} - 1, \quad (\text{B16})$$

$$\Theta = \phi \Theta_\ell + (1 - \phi) \Theta_s, \quad (\text{B17})$$

$$\Theta = \phi + \mathcal{H} - S \phi - G P_{\text{lith}}, \quad (\text{B18})$$

where $\theta^* = \frac{T_0}{\Delta T}$, $G = \frac{H \Delta \rho g}{\Delta T \gamma}$ is an inverse Clapeyron slope, $\Delta T = M \Delta C$, and P_{lith} is lithostatic pressure. Eq. (B18) is a quadratic equation that can be solved for porosity as a function of enthalpy and

Table B1. Parameters used in non-dimensional system of equations.

Parameter	Value	Name
δ	$\frac{1}{H} \left(\frac{K_0 \eta_0}{\mu} \right)^{\frac{1}{2}}$	Scaled compaction length
\mathcal{A}	$\frac{\alpha g H}{c_P}$	Adiabatic parameter
S	$\frac{\mathcal{L}}{c_P \Delta T}$	Stefan number
Pe_T	$\frac{H w_0}{\kappa}$	Thermal Peclet number
Pe_C	$\frac{H w_0}{D}$	Compositional Peclet number
κ	$\frac{k}{\rho_0 c_P}$	Thermal diffusivity
α^*	$\alpha \Delta T$	Reference thermal expansion coefficient
β^*	$\beta \Delta C$	Reference compositional expansion coefficient

bulk composition. Finally, the non-dimensional form of potential temperature is

$$\theta = (\tilde{\theta} + \theta^*)e^{A_z} - \theta^*. \quad (\text{B19})$$

APPENDIX C: FD-PDE FRAMEWORK

We use a new computational framework for finite-difference, staggered-grid discretization of partial differential equations (FD-PDE) that facilitates the development of testable and extensible code for (geodynamic) applications. The FD-PDE framework is layered over the Portable, Extensible Toolkit for Scientific Computation (PETSc, Balay *et al.* 2019). It leverages a new PETSc class for staggered grids, DMStag (Sanan *et al.* 2022). Governing equations are incorporated into FD-PDE as generic PDEs (i.e. FDPDEType); the user only specifies the coefficients (defined below), constitutive equations, and boundary conditions.

The FD-PDE framework allows flexibility in quickly building modular applications that are easily benchmarked. The framework was tested with a number of analytical solutions and community benchmarks, and using the method of manufactured solutions (MMS) to verify problems with non-linear coefficients (Roache 2002). Source code, documentation and tests for FD-PDE framework are available at <https://github.com/apusok/FD-PDE.git>.

The mechanical system of equations (eqs B6–B8) is solved separately from the energy and composition system of equations (eqs B12–B13). The mechanical system is discretized as FDPDE_StokesDarcy3Field type, and is a system of equations with three unknowns (\mathbf{u} , P , \mathcal{P}), written here in continuous form,

$$-\nabla P + \nabla \cdot [A_{SD}(\nabla \mathbf{u} + \nabla \mathbf{u}^T)] - \mathbf{B}_{SD} = \mathbf{0}, \quad (\text{C1})$$

$$\nabla \cdot \mathbf{u} + \nabla \cdot (D_2 \nabla P + \mathbf{D}_3 + D_4 \nabla \mathcal{P}) - C_{SD} = 0, \quad (\text{C2})$$

$$\nabla \cdot \mathbf{u} + D_1 \mathcal{P} - D_5 = 0, \quad (\text{C3})$$

where A_{SD} , B_{SD} , C_{SD} , $D_1 - D_5$ are FD-PDE coefficients to be specified by the user.

The energy–composition system is discretized as the FDPDE_Enthalpy type, and is a system of two equations

$$\begin{aligned} \frac{\partial \mathcal{H}}{\partial t} + A_1 \nabla \cdot T_p \mathbf{v} + B_1 \nabla \cdot (1 - \phi) \mathbf{v}_s \\ + \nabla \cdot C_1 \nabla T_p + D_1 = 0, \end{aligned} \quad (\text{C4})$$

$$\begin{aligned} \frac{\partial C^j}{\partial t} + A_2 \nabla \cdot (1 - \phi) \mathbf{v}_s C_s^j + B_2 \nabla \cdot \phi \mathbf{v}_\ell C_\ell^j \\ + \nabla \cdot C_2 \phi \nabla C_\ell^j + D_2 = 0, \end{aligned} \quad (\text{C5})$$

Table C1. FD-PDE coefficients used to solve system of equations for mechanics (PV) and energy and composition (HC).

Stokes–Darcy 3-field (<i>PV</i>)			Enthalpy (<i>HC</i>)		
A_{SD}	$\delta^2 \eta$	A_1	e^{-A_z}	A_2	1
B_{SD}	$(\phi + \mathcal{B}) \hat{\mathbf{k}}$	B_1	$-S$	B_2	1
C_{SD}	0	C_1	$-\frac{1}{Pe_T} e^{-A_z}$	C_2	$-\frac{1}{Pe_C}$
D_1	$-\frac{1}{\delta^2 \xi}$, where $\xi = \zeta - \frac{2}{3} \eta$	D_1	0	D_2	0
D_2	$-K$				
D_3	$-K(1 + \mathcal{B}_\ell) \hat{\mathbf{k}}$				
D_4	$-K$				
D_5	0				

where the unknowns are enthalpy \mathcal{H} , primary temperature variable T_p (taken as potential temperature), and concentration of component j in the bulk C^j . Other variables are T is secondary temperature variable (taken as normal temperature), ϕ is porosity and $C_{\ell,s}^j$ are liquid and solid concentrations of component j and are obtained by the enthalpy method. The A_k , B_k , C_k , D_k symbols are FD-PDE coefficients that must be specified by the user. The velocities \mathbf{v} , \mathbf{v}_s , \mathbf{v}_ℓ are also FD-PDE coefficients; they represent the solutions for bulk, solid and liquid velocity obtained from the Stokes–Darcy system.

The FD-PDE coefficients for conservation of mass and momentum (FDPDE_StokesDarcy3Field), and conservation of energy and composition (FDPDE_Enthalpy) used in the model here are given in Table C1.

C1 Model setup, boundary conditions and melt extraction

Dirichlet and Neumann boundary conditions can be imposed within the FD-PDE framework (i.e. the framework contains templates for BC_DIRICHLET and BC_NEUMANN). Other uses of linear or non-linear boundary conditions are possible, but the user needs to construct them case by case.

Melt extraction at the mid-ocean ridge is implemented within a small distance from the ridge axis ($|x| \leq x_{MOR}$) in a horizontal window at the top of the domain. We first set enthalpy boundary conditions $\frac{\partial \mathcal{H}}{\partial z} = 0$ for $|x| \leq x_{MOR}$. In addition, we impose a reduced permeability within the extraction window, by limiting porosity on the top boundary to be

$$\phi_{top} = f \phi_{centre}, \quad (\text{C6})$$

$$K_{top} = K_0 f^n \phi_{centre}^n, \quad (\text{C7})$$

where ϕ_{top} is porosity on the top edge of domain, ϕ_{centre} is calculated porosity in centre cells and f is an extraction efficiency parameter. This operation is allowed in the staggered grid finite difference

discretization, which requires by default interpolation of porosity from centre cells to edges. We use a value of $f = 0.2$, which yields crustal thicknesses of 5–12 km.

APPENDIX D: SCALING ANALYSIS

Buoyancy-driven convection is generally studied in terms of the dimensionless Rayleigh number, which is the ratio of factors driving convection to those resisting it. Spiegelman (1993) derived a similar parameter to the Rayleigh number for the mantle flow beneath MORs where buoyancy forces arise from the presence of melt (i.e. porous buoyancy). Katz (2010) gave a more detailed consideration of this number. Here, we use a similar approach to include the effect of composition and temperature.

Starting from the momentum equation of the aggregate (A3), we write the buoyancy term to depend on ϕ , $\rho_{s0} = \rho_0$, $\Delta\rho = \rho_{s0} - \rho_{\ell 0}$, $\Delta C = C_s - C_\ell$, $F = \frac{C_s - C_0}{\Delta C}$, and $\tilde{T} = T - T_0$ as follows:

$$\phi \Delta\rho + \overline{\rho_0 B} = \phi \Delta\rho + (\rho_0 - \phi \Delta\rho) \beta F \Delta C - (\rho_0 - \Delta\rho) \phi \beta \Delta C + (\rho_0 - \phi \Delta\rho) \alpha \tilde{T}. \quad (D1)$$

Next, we assume a constant viscosity, $\eta = \eta_0$, a simplification applied only in the scaling analysis, and we take the curl of eq. (A3) to obtain

$$\eta_0 \nabla^2 \omega = g[\Delta\rho - \Delta\rho \beta \Delta C F - (\rho_0 - \Delta\rho) \beta \Delta C - \Delta\rho \alpha \tilde{T}] \partial_x \phi + g(\rho_0 - \phi \Delta\rho) \beta \Delta C \partial_x F + g(\rho_0 - \phi \Delta\rho) \alpha \partial_x \tilde{T}, \quad (D2)$$

where $\hat{\omega} \mathbf{j} = \nabla \times \mathbf{v}_s$ is vorticity and ∂_x represents the partial derivative of a quantity in the x direction. The above equation is the vorticity equation and states that lateral gradients in porosity, composition and temperature are an internal source of vorticity. We use the following scales, shown schematically in Fig. 1(b), to non-dimensionalize the equation

$$[x] = h_0, \quad [\omega] = \frac{U_0}{h_0}, \quad [\phi] = \phi_0, \quad [F] = F_0, \quad [\tilde{T}] = \Delta T, \quad (D3)$$

where h_0 is the maximum height of melting column, ϕ_0 is characteristic melt fraction, F_0 is degree of melting at top of the column, U_0 is half-spreading rate and ΔT is temperature difference defined via the phase diagram. The non-dimensionalized vorticity equation becomes

$$\nabla^2 \omega = v_\phi \partial_x \phi + v_C \partial_x F + v_T \partial_x \tilde{T}, \quad (D4)$$

where

$$v_\phi = \phi_0 [\Delta\rho - \beta \Delta C (F_0 \Delta\rho + \rho_0 - \Delta\rho) - \Delta\rho \alpha \Delta T] g \times \frac{h_0^2}{\eta_0 U_0}, \quad (D5)$$

$$v_C = (\rho_0 - \phi_0 \Delta\rho) \beta \Delta C F_0 g \frac{h_0^2}{\eta_0 U_0}, \quad (D6)$$

$$v_T = (\rho_0 - \phi_0 \Delta\rho) \alpha \Delta T g \frac{h_0^2}{\eta_0 U_0}, \quad (D7)$$

are dimensionless buoyancy numbers. We use an expression for characteristic porosity ϕ_0 from Ribe (1985) to expand the buoyancy number due to porosity as

$$v_\phi = \left[\frac{\mu W_0 F_0}{K_0 \Delta\rho g} \right]^{1/3} [\Delta\rho - \beta \Delta C (F_0 \Delta\rho + \rho_0 - \Delta\rho) - \Delta\rho \alpha \Delta T] g \times \frac{h_0^2}{\eta_0 U_0} \quad (D8)$$

where μ is the viscosity of the magma, F_0 is degree of melting at the top of melting column, W_0 is passive rate of mantle upwelling, K_0 is the permeability prefactor and n is permeability exponent, taken equal to 3 in this study.

When $\alpha = 0$ and $\beta = 0$ (no compositional and thermal buoyancy), the porous buoyancy number reduces to $v_\phi = \phi_0 \Delta\rho g h_0^2 / \eta_0 U_0$ as in Spiegelman (1993) and Katz (2010).

APPENDIX E: PETROLOGICAL MODELLING

The compositional density change in eq. (1) is modulated by β , the coefficient of chemical expansion. Since the equation of state linearizes the effect of Fe/Mg partitioning (with C loosely representing the Mg#), we estimate a best-fitting value of β using the thermodynamics software pMELTS (Ghiorso *et al.* 2002) from the ThermoEngine/ENKI software ecosystem (Ghiorso & Wolf 2019).

In a partial-melt system, density changes can be due to temperature (T), pressure (P), composition (C), mineralogy (M , through reactions and changes in modal proportion of minerals) and volume fraction of melt (ϕ , porosity) (Schutt & Leshner 2006). The total density change of a given phase (liquid or mineral phase) can be written as

$$d\rho = \frac{\partial\rho}{\partial X_i} dX_i, \quad (E1)$$

where X_i can be T , P , C , M , ϕ . To simplify the problem, we only consider temperature, pressure and composition (Mg#) as the main factors on density change. We then use pMELTS to obtain phase densities and properties during melting, and determine the compositional effect on density. We consider three simplified melting experiments: isobaric, isothermal and isentropic (Fig. E1).

1. Melting under isobaric conditions. The density change for a given phase is

$$d\rho = \left(\frac{\partial\rho}{\partial T} \right)_P dT + \left(\frac{\partial\rho}{\partial C} \right)_P dC, \quad (E2)$$

where the following coefficients are defined

$$\alpha = -\frac{1}{\rho} \left(\frac{\partial\rho}{\partial T} \right)_P, \quad (E3)$$

$$\beta_P = -\frac{1}{\rho} \left(\frac{\partial\rho}{\partial C} \right)_P, \quad (E4)$$

with α the coefficient of thermal expansion and β_P the coefficient of chemical expansion at isobaric conditions. Integrating eq. (E2) under the assumption of constant expansion coefficients, we obtain the density equation of state

$$\rho = \rho_0 [1 - \alpha(T - T_0) - \beta_P(C - C_0)], \quad (E5)$$

where we used the Taylor-series approximation $e^a \approx 1 + a$ for $a \ll 1$ since density changes are small relative to the density itself. An effective β_P for the solid and liquid phases under isobaric conditions is obtained by fitting the above equation to the results of pMELTS calculations (Fig. E2 and Table E1).

2. Melting under isothermal conditions. The density change for a given phase is now given by

$$d\rho = \left(\frac{\partial\rho}{\partial P} \right)_T dP + \left(\frac{\partial\rho}{\partial C} \right)_T dC, \quad (E6)$$

where the following coefficients are defined

$$k_T = \frac{1}{\rho} \left(\frac{\partial\rho}{\partial P} \right)_T, \quad (E7)$$

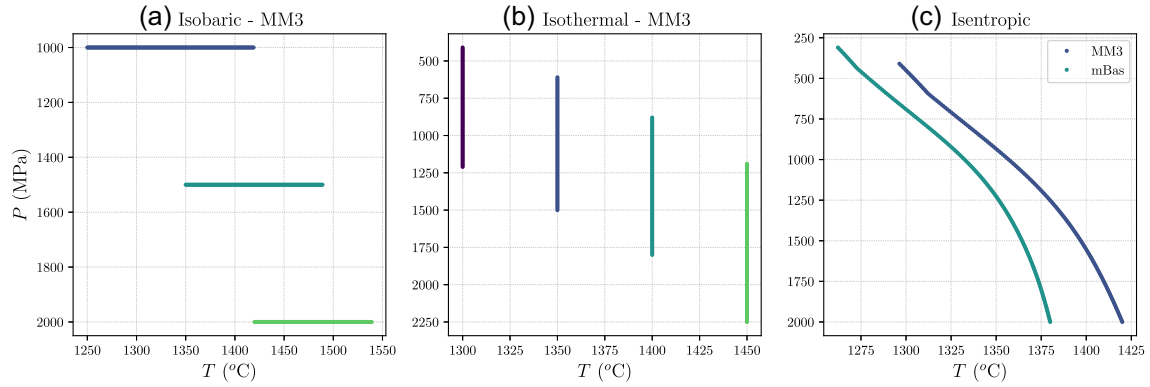


Figure E1. Melting curves in P – T space used in pMELTS simulations. (a) Isobaric conditions for MM3 bulk composition. (b) Isothermal conditions for MM3 bulk composition. (c) Isentropic (adiabatic) conditions for MM3 and mBas bulk compositions. Each line represents a different experiment.

Table E1. Summary of pMELTS calculations to determine β , the coefficient of chemical expansion. Bulk solid values ($\beta^{\#1}$, $\beta^{\#2}$) are calculated in two ways (see pMELTS method). Bulk compositions for MM3 (Mg# 0.913, Baker & Stolper 1994) and mBas (Mg# 0.897) are given below calculations of β .

Rock type	P (GPa)	T (°C)	Melt fraction (ϕ)	β (liquid)	$\beta^{\#1}$ (solid)	$\beta^{\#2}$ (solid)	$\Delta\rho/\rho$ per 1% melting (solid)	$\Delta\rho/\rho$ due to chemical depletion per 1% melting (solid)
<i>Isobaric conditions</i>								
MM3	1.0	1250–1420	0.0045–0.3001	2.2072	0.7835	0.9961	–0.0552	–0.0283
MM3	1.5	1350–1490	0.0037–0.2994	3.3050	0.6264	0.4688	–0.0547	–0.0322
MM3	2.0	1420–1540	0.0010–0.2950	–4.9170	0.5399	0.3500	–0.0539	–0.0044
<i>Isothermal conditions</i>								
MM3	1.210–0.400	1300	0.0055–0.2981	4.1262	0.7138	0.7445	–0.0399	–0.0198
MM3	1.500–0.600	1350	0.0037–0.3078	–5.8704	0.6643	0.5224	–0.0439	–0.0226
MM3	1.800–0.870	1400	0.0043–0.3035	–1.5537	0.6312	0.8844	–0.0485	–0.0262
MM3	2.225–1.180	1450	0.0005–0.3046	–0.4704	0.5944	0.5570	–0.0544	–0.0539
<i>Isentropic conditions</i>								
MM3	2.0–0.4	1420 (start)	0.0010–0.2916	0.3045	0.4963	0.6489	–0.0395	–0.0200
mBas	2.0–0.3	1380 (start)	0.0015–0.2810	–6.7550	0.5539	0.8816	–0.0427	–0.0183
<i>Bulk compositions</i>								
MM3	SiO ₂ : 45.47 TiO ₂ : 0.11 Al ₂ O ₃ : 4.00 Fe ₂ O ₃ : 0.68 Cr ₂ O ₃ : 0.68 FeO : 6.61 MnO : 0.00 H ₂ O : 0.00							
	MgO : 38.53 NiO : 0.00 CoO : 0.00 CaO : 3.59 Na ₂ O : 0.31 K ₂ O : 0.00 P ₂ O ₅ : 0.00							
mBas	SiO ₂ : 45.26 TiO ₂ : 0.19 Al ₂ O ₃ : 3.88 Fe ₂ O ₃ : 0.40 Cr ₂ O ₃ : 0.41 FeO : 7.81 MnO : 0.00 H ₂ O : 0.00							
	MgO : 37.85 NiO : 0.00 CoO : 0.00 CaO : 3.57 Na ₂ O : 0.30 K ₂ O : 0.01 P ₂ O ₅ : 0.00							

$$\beta_T = -\frac{1}{\rho} \left(\frac{\partial \rho}{\partial C} \right)_T, \quad (\text{E8})$$

with k_T the isothermal compressibility and β_T the coefficient of chemical expansion at isothermal conditions. The linearized density equation of state becomes

$$\rho = \rho_0(1 + k_T(P - P_0) - \beta_T(C - C_0)). \quad (\text{E9})$$

In a similar way to above, we determine an effective β_T for the solid and liquid phases under isothermal conditions (Fig. E3 and Table E1).

3. Melting under isentropic conditions. The density change for a given phase is given by

$$d\rho = \left(\frac{\partial \rho}{\partial P} \right)_s dP + \left(\frac{\partial \rho}{\partial T} \right)_s dT + \left(\frac{\partial \rho}{\partial C} \right)_s dC, \quad (\text{E10})$$

where the following coefficients are defined

$$k_s = \frac{1}{\rho} \left(\frac{\partial \rho}{\partial P} \right)_s, \quad (\text{E11})$$

$$\alpha_s = -\frac{1}{\rho} \left(\frac{\partial \rho}{\partial T} \right)_s, \quad (\text{E12})$$

$$\beta_s = -\frac{1}{\rho} \left(\frac{\partial \rho}{\partial C} \right)_s, \quad (\text{E13})$$

with k_s the isentropic compressibility, α_s the isentropic coefficient of expansion, and β_s the coefficient of chemical expansion at isentropic conditions. The density equation of state becomes

$$\rho = \rho_0(1 + k_s(P - P_0) - \alpha_s(T - T_0) - \beta_s(C - C_0)), \quad (\text{E14})$$

We determine an effective β_s for the solid and liquid phases under isentropic conditions (Fig. E4 and Table E1).

4. pMELTS methods and results. We use a fertile lherzolite composition based on the Kilbourne Hole xenolith MM3 (Mg# 0.913; Baker & Stolper 1994) for the isobaric, isothermal and isentropic melting experiments, and a more basaltic composition, mBas (Mg# 0.897) for isentropic experiments.

Major-element compositions of MORBs (Langmuir *et al.* 1992) indicate that silicate melting initiates at a depth of about 60–65 km. Therefore, we are interested in melting depths relevant for MORs (<60 km, ~2 GPa) and we run pMELTS simulations with different melting paths assuming batch melting

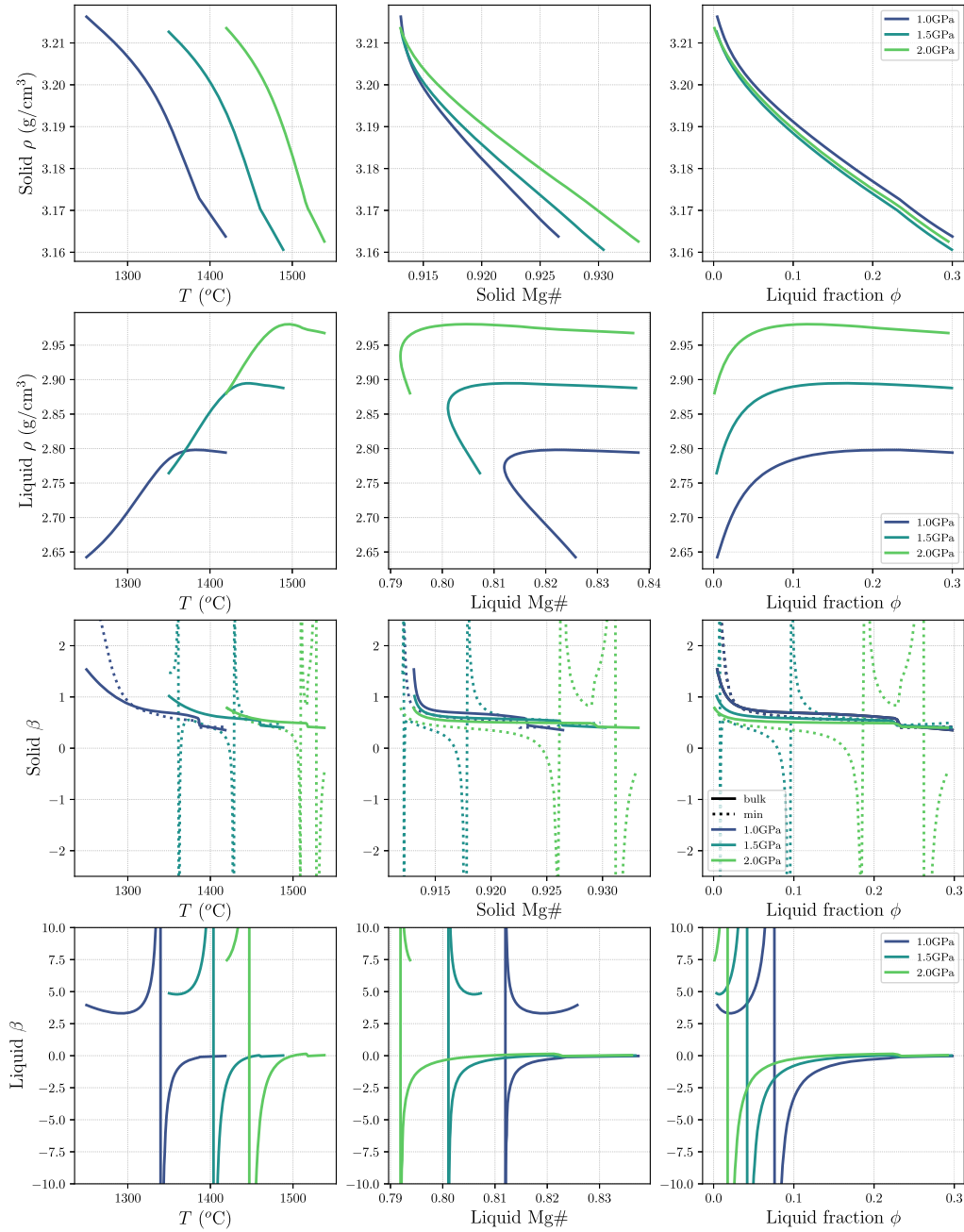


Figure E2. Density variations and β_P for liquid and solid (bulk) phases as function of temperature, Mg# and liquid fraction in pMELTS calculations under isobaric conditions. Continuous lines in solid β_P represent bulk averaged calculations, while dotted lines represent mineral calculations.

(see Fig. E1 for melting curves). To include the clinopyroxene-out criterion (consumed at about 24.5 % liquid fraction), approximately maximum 30 % liquid fraction is considered in our calculations.

At each pMELTS iteration during a melting simulation, we extract the following properties for all phases: T , P , weight fraction, ρ , Mg# (calculated from oxide weight components), and coefficients of density change (α , k). We then calculate the bulk properties of the solid phase. Solid phase includes all mineral phases present in the system, such as olivine, spinel, orthopyroxene and clinopyroxene.

The calculation of β for the liquid phase is straightforward, while the calculation for the solid phase can be performed in two ways.

(i) Apply density equation on solid-aggregate properties. An example for isobaric conditions calculates

$$\bar{\rho} = \frac{\sum x_m}{\sum \frac{x_m}{\rho^m}}, \quad (\text{E15})$$

$$\bar{\alpha} = \sum x_m \alpha^m, \quad (\text{E16})$$

$$\overline{\text{Mg\#}} = \frac{X_{\text{MgO}}^{\text{solid}}}{X_{\text{FeO}}^{\text{solid}} + X_{\text{MgO}}^{\text{solid}}}, \quad (\text{E17})$$

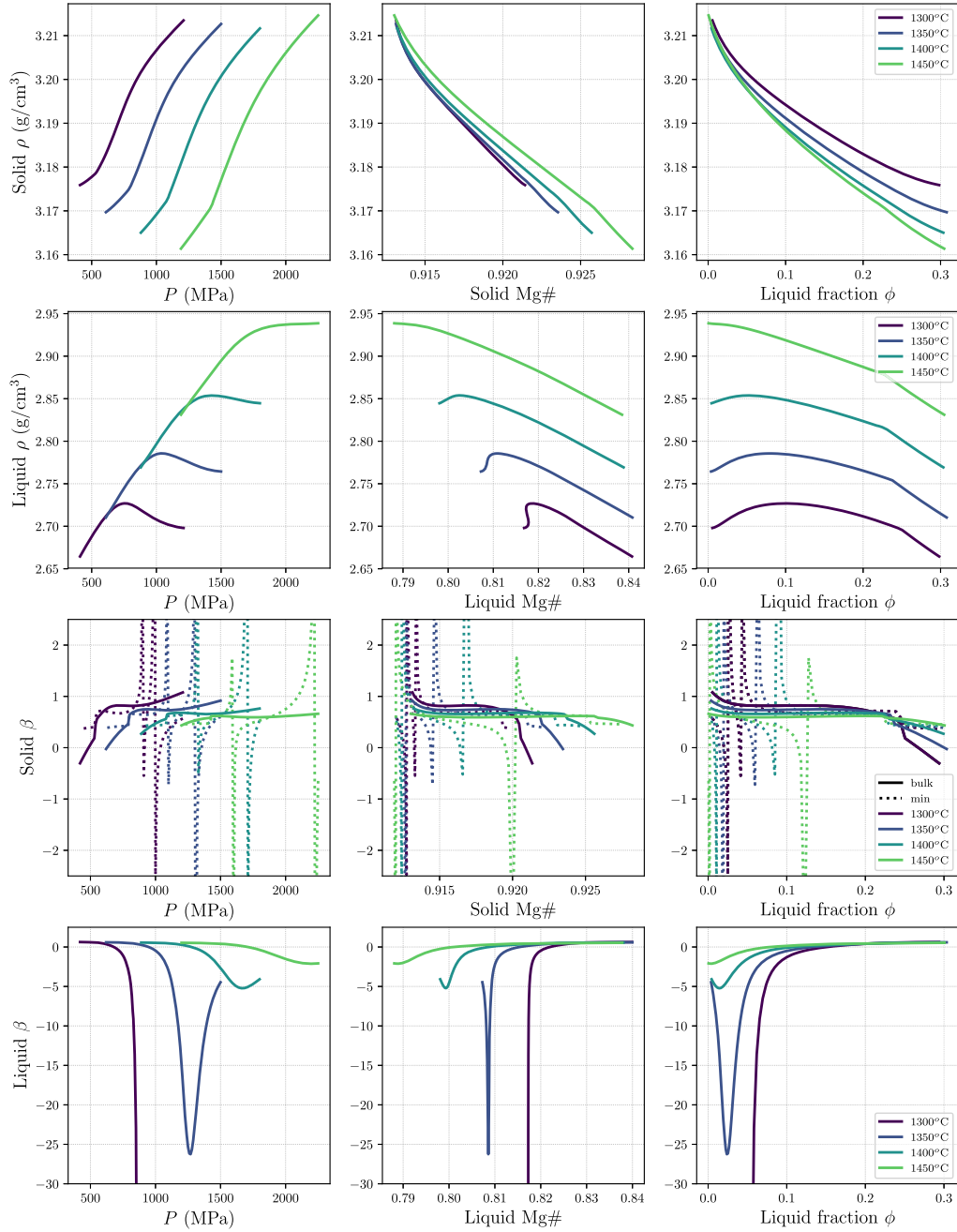


Figure E3. Density variations and β_T for liquid and solid (bulk) phases as function of temperature, Mg# and melt fraction in pMELTS calculations under isothermal conditions.

$$\bar{\beta} = \frac{1}{\text{Mg}\# - \text{Mg}\#_0} \left(1 - \frac{\bar{\rho}}{\rho_0} - \bar{\alpha}(T - T_0) \right) \quad (\text{E18})$$

where bar properties have been averaged for all solid mineral phases m , and x_m is weight fraction. This method is plotted with continuous lines and labelled as ‘bulk’ in Figs E2–E4.

(ii) Apply density equation per mineral phase, and then calculate a solid-aggregate β . Example for isobaric conditions calculates

$$\rho^m = \rho_0^m (1 - \alpha^m(T - T_0) - \beta^m(\text{Mg}\#^m - \text{Mg}\#_0^m)), \quad (\text{E19})$$

$$\bar{\beta} = \sum x_m \beta^m, \quad (\text{E20})$$

where m represents solid mineral phase, and x_m is weight fraction. This method is plotted with dotted lines and labelled as ‘min’ in Figs E2–E4.

The first method is preferred for an estimate of β (i.e. $\beta^{\#1}$ in Table E1). The reason is that calculations for mineral parameter values become highly uncertain at low weight fractions, which produce the spikes in Figs E2–E4.

Under all three experimental setups, solid density decreases monotonically with increasing melt fraction. In contrast, liquid density increases at low melt fractions (Fe and other incompatible elements preferentially partition into the melt phase) then reaches a maximum that coincides with the minimum Mg#. After this point,

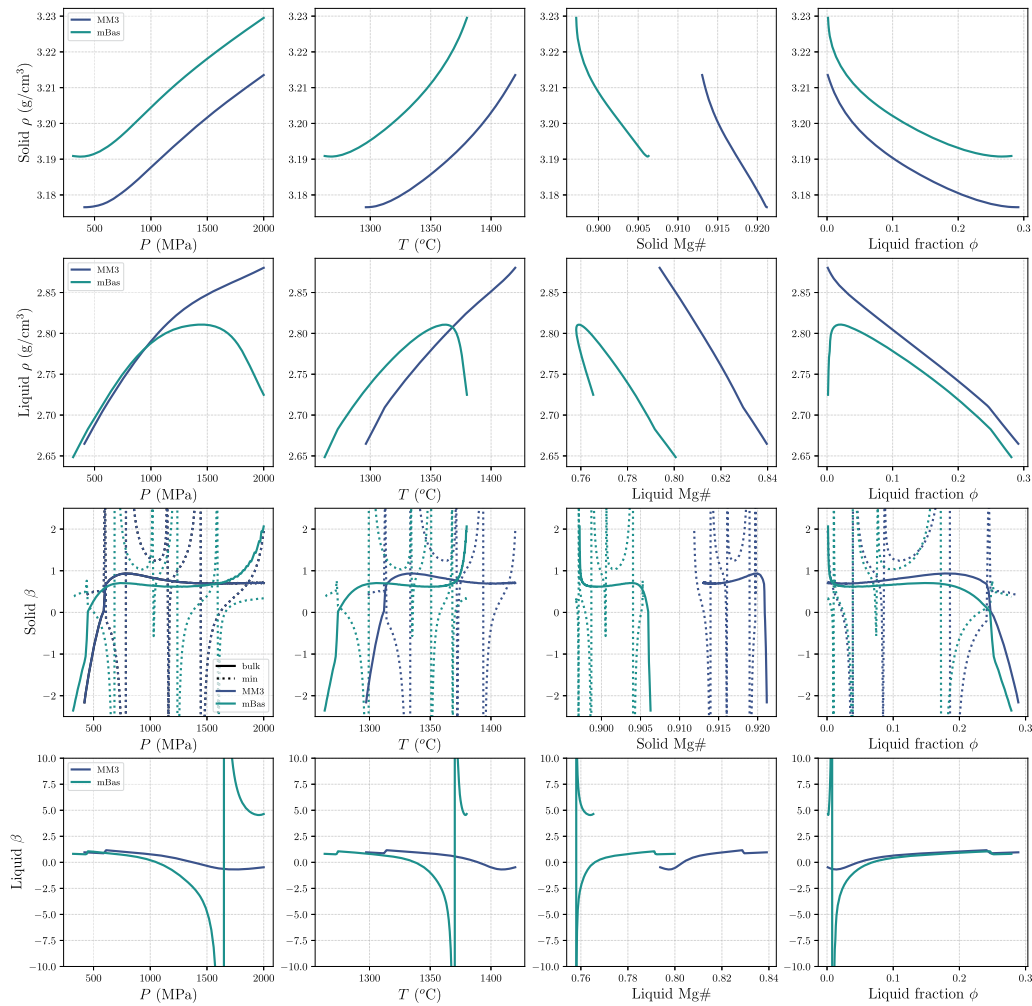


Figure E4. Density variations and β_S for liquid and solid (bulk) phases as function of temperature, Mg# and melt fraction in pMELTS calculations under isentropic (adiabatic) conditions.

liquid density decreases due to transfer of Mg and lighter elements into the liquid phase.

The petrological calculations can be reproduced using the Jupyter notebooks provided in the data repository: `MOR_beta_revised.ipynb` and `MOR_beta_revised_min.ipynb`.

The notebooks require the `equilibrate` module provided by ThermoEngine/ENKI. Finally, fractional melting calculations, which are more appropriate for the natural system, may modify the estimates of β obtained here (Afonso & Schutt 2012).